

# Representational Drift and Learning-Induced Stabilization in the Olfactory Cortex

Guillermo B. Morales<sup>1</sup>, Miguel A. Muñoz<sup>1,✉</sup>, and Yuhai Tu<sup>2,✉</sup>

<sup>1</sup>Departamento de Electromagnetismo y Física de la Materia and Instituto Carlos I de Física Teórica y Computacional, Universidad de Granada, E-18071 Granada, Spain  
<sup>2</sup>IBM T. J. Watson Research Center, Yorktown Heights, NY 10598

**The brain encodes external stimuli through patterns of neural activity, forming internal representations of the world. Recent experiments show that neural representations for a given stimulus change over time. However, the mechanistic origin for the observed “representational drift” (RD) remains unclear. Here, we propose a biologically-realistic computational model of the piriform cortex to study RD in the mammalian olfactory system by combining two mechanisms for the dynamics of synaptic weights at two separate timescales: spontaneous fluctuations on a scale of days and spike-time dependent plasticity (STDP) on a scale of seconds. Our study shows that, while spontaneous fluctuations in synaptic weights induce RD, STDP-based learning during repeated stimulus presentations can reduce it. Our model quantitatively explains recent experiments on RD in the olfactory system and offers a mechanistic explanation for the emergence of drift and its relation to learning, which may be useful to study RD in other brain regions.**

Neural representations | Representational drifts | Neural networks | Olfactory system | Synaptic plasticity  
 Correspondence: [mamunoz@onsager.ugr.es](mailto:mamunoz@onsager.ugr.es) [yuhai@us.ibm.com](mailto:yuhai@us.ibm.com)

## Introduction

The brain is a powerful computing machine, “trained” by millions of years of evolution to process, represent, and interpret the thousands of incoming stimuli it is exposed to on a daily basis. The prevailing hypothesis suggests that the brain encodes information about such external inputs through patterns of neural spiking activity in sensory areas, often observed to reside within lower-dimensional manifolds (1–3), which constitute an internal representation of the external world (4, 5).

Nevertheless, when observed, the ubiquitous “drift” of neural codes seems to differ in its properties across brain regions. For instance, despite the measured changes at the single-cell level, overall population statistics have been shown to remain invariant across weeks in the piriform cortex (6) and posterior parietal cortex (7), whereas in the hippocampus, drift at relatively short timescales of hours is associated with an increased sparsification of the population response (8, 9). Similarly, neural population responses to drifting gratings in mouse visual cortex have been shown to be stable across weeks, while encoding of natural movies in the same region appeared to change considerably across weeks, indicating the existence of a stimulus-dependent drift in visual cortex (10). In contrast, drift rate in olfactory cortex was demonstrated to be fairly independent of the chemical nature of the odor but, remarkably, it could be slowed down by in-

creasing the frequency of stimulus presentation (6).

Representational drift (RD) is generally believed to be caused by changes at the synaptic level, which are difficult to measure, especially in behaving animals. Several recent studies have thus focused on studying RD by using computational approaches to model the dynamics of synaptic weights. In particular, several hypotheses have been investigated regarding the origin of RD, including: i) spike timing-dependent plasticity (STDP) or synaptic turnover, in combination with homeostatic normalization of synaptic weights (11); ii) noisy synaptic-weight updates with white (12) or correlated (13) noise; iii) node or weight dropout (14); and iv) implicit regularization of the population activity (9). Alternatively, it has been recently proposed that RD could be driven by fluctuations in the intrinsic excitability of neurons, rather than changes at the synaptic level (15).

In this paper, we focus on the mammalian olfactory cortex, for which new experimental findings on RD have been recently reported by Schoonover and colleagues using mice (6). To draw a quantitative comparison with their experimental results, we develop a biologically realistic computational model of the mouse olfactory cortex, showing that a simple multiplicative stochastic process over the synaptic weights can account for the observed drift in the representation of odors, while naturally giving rise to the empirically measured log-normal distribution of weights and stable population statistics. Furthermore, our model can also explain why RD slows down when the frequency of stimulus presentation increases, as recently observed in experiments (6).

To the best of our knowledge, our model provides the first quantitative explanation of the observed drift in the olfactory system. More importantly, an intuitive mechanistic picture emerges in which RD is caused by slow and spontaneous fluctuations in synaptic weights, while learning at a faster timescale drives the system deterministically towards a low-dimensional representation manifold, which effectively suppresses RD. We found that this general mechanistic picture, although applied here in a relatively realistic model of the olfactory cortex, could also be useful in understanding RD in other regions of the brain.

## The background: Odor encoding in the olfactory cortex

To provide additional context for the problem, we first present an overview of the processes involved in odor per-

ception in the mouse olfactory cortex, focusing on the neural architecture that underlies the internal representations of odors (see, for instance, (16) for a recent review).

Odor perception begins when volatile molecules in the environment, known as odorants, bind to receptors in *olfactory sensory neurons* (OSNs) of the nasal epithelium during inhalation (see sketch in Fig. 1a). The pioneering work of Buck and Axel, back in 1991, revealed that each OSN in the mouse expressed just one out of  $\sim 1000$  different odorant receptor genes (17). Although these receptors exhibit high affinity for specific odorants, they are broadly tuned and can also bind to other volatile compounds with lower affinity. Nonetheless, olfactory sensory neurons (OSNs) with the highest affinity receptors for a particular odorant at a given concentration consistently fire first upon its presentation (18, 19).

During the next step of odor processing, all OSNs expressing the same type of receptor project their axons onto a unique set of glomeruli in the olfactory bulb (OB) (20, 21) (Fig. 1a). These spheroidal structures host the synaptic connections between the OSN axon terminals and the dendrites of the secondary neurons: the *mitral/tufted cells* (MTCs). For a given odorant, although OSNs with less specific receptors can be eventually activated, the MTCs associated with the most odorant-specific receptors will fire the earliest, effectively transforming the initial receptor-specific encoding into a temporal encoding in the OB.

The information encoded in temporal patterns of MTCs activity in the OB is conveyed through random and overlapping *lateral olfactory track* (LOT) connections into the piriform cortex (PCx), i.e., the *temporal* encoding in the OB is further translated into an *ensemble* code in the PCx, where odorant identity is determined by specific sets of principal neurons (pyramidal cells, mainly) recruited during the sniff (22). Importantly, cortical odor responses are mostly determined by the earliest-active glomeruli (the ones with higher specificity for the given odorant) due to the fast recruiting of inhibitory interneurons (feed-forward inhibitory neurons (FFINs) and feed-back inhibitory neurons (FBINs), see Fig. 1a) that suppress the cortical response to later, less-specific OB inputs (22–25). For simplicity, in the following results we will not distinguish between "odors" and "odorants" and will use both terms indistinctly.

## The modeling framework

**A spiking network model of the olfactory cortex.** In order to make direct comparison with experiments, we developed a realistic model of the olfactory bulb (OB) and piriform cortex (PCx) based on the spiking network model proposed by Stern *et al.* (22). As illustrated in Fig. 1c, the pyramidal neurons (PYRs) in PCx receive excitatory inputs directly from MTCs through LOT connections as well as recurrent connections with other pyramidal cells. The PYRs are also subject to inhibitory currents from FBIN and FFIN neurons, which receive excitatory inputs from PYRs and MTCs, respectively.

RD occurs in a timescale of days, which is  $\sim 10^4 \times$  longer

than the timescale studied in (22) for fixed synaptic weights. To make computation for such long time scales feasible, we reduced the number of neurons in our model but compensated it by increasing the connectivity so that, for each type of neuron, the average incoming excitatory and inhibitory currents remain the same as in (22) so that the network remains balanced (see Methods and Fig. S.1j for details). The relative values of all network parameters (membrane timescales, average synaptic weights, fraction of responsive glomeruli, etc.) were kept as in (22). Following Stern *et al.* (22), each respiration cycle consisted of an inhalation period of duration  $\tau_{inh} = 200\text{ms}$  followed by an exhalation period of duration  $\tau_{exh} = 300\text{ms}$  (see Fig. 1b). MTCs respond with an enhanced firing rate to the presence of an odor only in the inhalation period. An example of the emergent pattern of MTC activity during the presentation of a particular odor is given in Fig. S.1a. To account for the baseline resting-state activity observed in the PCx in the absence of odor inputs, we included random Poissonian spiking of all pyramidal neurons at a relatively slow rate  $f_{spont} = 1\text{Hz}$  (see Fig. S.1a).

**Modeling dynamics of synaptic plasticity.** The key new ingredient we introduced in our model is synaptic plasticity. Empirical evidence on the fundamental role of synaptic modifications in different parts of the olfactory cortex (26–31) suggests that synaptic plasticity is the most plausible origin for RD. However, in order to explain the observed RD behaviors in olfactory system, the responsible synaptic plasticity mechanisms need to satisfy several constraints: **(i)** give rise to stable log-normal-distributed values of the synaptic efficiencies, as it has been extensively documented by both *in vivo* and *in vitro* experiments (32, 33); **(ii)** operate on a "slow" intrinsic time scale of days or weeks, in agreement with the observed time scale of the drift in the olfactory cortex (6); **(iii)** lead to drifting representations of inputs across time; **(iv)** guarantee the empirically-observed invariance of population statistics despite the changing representations of the stimuli; and **(v)** explain the observed dependence of the drift rate with the frequency of stimulus presentation (6). In our model, we incorporate a combination of two synaptic plasticity mechanisms that, together, can satisfy these constraints.

**I. The slow stochastic synaptic dynamics.** It was shown by Loewenstein *et al.* (32) that dendritic spines in the auditory cortex of mice exhibited substantial changes in size at timescales that ranged, precisely, from days to months. Moreover, not only could the stationary probability distribution of spine sizes be very well fitted by a log-normal distribution, but also the magnitude of change in spine sizes was found to be proportional to the size of the spines, hinting at the existence of an underlying multiplicative dynamics (32). Inspired by these empirical findings, we propose to model the *slow* dynamics of synaptic weights as a *geometric mean-reversion* (GMR) stochastic process<sup>1</sup>:

$$\dot{J}(t) = \omega(\mu - J(t)) + \sigma J(t)\xi(t), \quad (1)$$

<sup>1</sup>In order to preserve the sparsity in the connectivity matrices, only changes in already existing synapses were allowed.

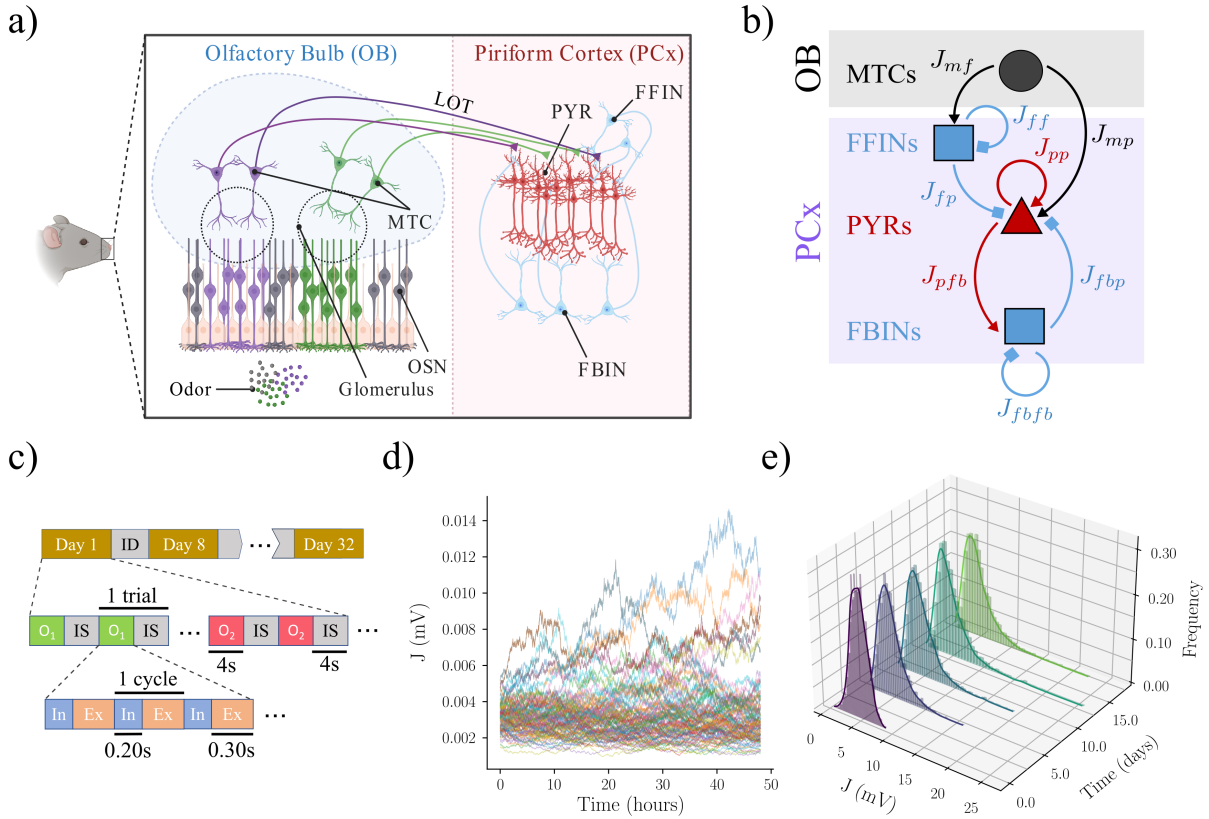


**Fig. 1. Model and experimental setup.** (a) When a given odor reaches the nasal epithelium, the different odorants composing it (green, purple and gray molecules in the figure) bind to specific receptors in olfactory sensory neurons (OSNs). Next, OSNs expressing the same type of odorant receptor project their axons into the same glomerulus, where they connect to the dendrites of mitral/tufted cells (MTCs). Random projections of MTCs axons into the piriform cortex (PCx) conform the lateral olfactory track (LOT). In the PCx pyramidal (PYR) neurons receive excitatory inputs from MTCs, as well as inhibitory connections from FFINs and FBINs. Illustration created using the BioRender software. (b) Diagram of the model, depicting the different types of neural populations considered and their interactions. (c) Testing protocol for PCx responses to odor presentation, following the experimental setup in (6). For each test day and trial, an odor  $O_i$  is presented for 4s, followed by an inter-stimuli (IS) transient of the same duration. During odor presentation, the spiking frequency of MTCs change during the inhalation (IN) and exhalation (EX) periods that constitute one respiration cycle (see main text). Test days are spaced in time by inter-days (ID) transients lasting 8 days. (d) Trajectories of 100 randomly chosen weights between MTCs and pyramidal neurons under the GMR process. (e) Evolution of the probability distribution for the MTC-to-pyramidal weights, showing how an original Gaussian shape evolves towards a lognormal distribution.

where  $J$  represents a non-zero synaptic weight between two neurons,  $\mu$  is the average value of the associated stationary log-normal weight distribution,  $\xi(t)$  is a zero-mean, unit variance, Gaussian white noise, and  $\omega$  and  $\sigma$  are constants for the deterministic force and noise terms, respectively<sup>2</sup>. As an illustration, Fig. 1d highlights the stochastic evolution of some LOT weights under our proposed rule, whereas Fig. 1e shows how multiplicative fluctuations evolve an initially Gaussian distribution for the weights towards a heavy-tailed (lognormal) stationary distribution.

**II. The fast stimulus-dependent synaptic dynamics.** From the Schoonover et al work (6), the drift rate for representations of previously “learned” odors decreases with the frequency of stimulus presentation. This suggests the existence of a second mechanism concomitant to the previous one, operating on a much faster time scale of seconds (i.e., on the scale of the stimulus presentation). In this paper, we implemented a multiplicative STDP learning rule as proposed in (34) (see

<sup>2</sup>It is shown in the SI that this synaptic plasticity mechanism can be approximated to a simplified version of the phenomenological one proposed by Loewenstein et al. (32).

Methods for details), which can alter synapses on a “fast” time scale during odor presentation.

For simplicity, we only implement these two synaptic plasticity mechanisms in mitral-to-pyramidal (LOT) and pyramidal-to-pyramidal (recurrent) connections, while synaptic weights involving inhibitory neurons remain fixed. Furthermore, we neglect the effect of STDP during transient time without stimulus due to the fact that the background activity due to random sparse inputs from baseline activity at the MTCs and low-rate random Poissonian spiking of pyramidal neurons (Fig. S.1a) is very small. For the same reason, given that the time spanned between test days is several orders of magnitude greater than the timescale of stimuli presentation, we also neglect the effect of the slow GMR process during the short periods of odor presentation.

**Mimicking the experimental setup.** In order to compare the results from computational analyses of our model with existing empirical evidence, we aimed at reproducing the experimental setup and analyses used by Schoonover et al. (6).

Prior to the beginning of the experiment, we let MTC-to-pyramidal and pyramidal-to-pyramidal weights stochasti-

cally evolve under Eq. 1 for 32 days, to ensure that a quasi-stationary weight distribution was reached (see Fig. 1d and Fig. S.1b). Then, following the experimental study, the total simulated experiment consisted of 32 days during which the network dynamics is driven solely by the spontaneous pyramidal and MTCs activity. At 8-day intervals, a test period is included during which 8 different odors are sequentially presented. More specifically, each odor is presented 7 times (trials) during each test period, spanning 8 respiration cycles (4s) in each trial, followed by a 4s inter-odor transient between trials (see Fig. 1b).

For our analysis, we only consider neurons that show significant trial-averaged response over baseline activity to at least one odor in one day (Wilcoxon rank-sum test,  $\alpha = 0.005$ ). Specifically, for each test day  $d$ , odor  $o$  and trial  $m$ , we averaged pyramidal responses in time across 2 two-second windows after odor onset, then subtracted for each neuron its average baseline spontaneous rate to construct population firing rates,  $\mathbf{x}_{d,o,m} \in \mathbb{R}^{2N_{PYR}}$ . Unless otherwise stated, all measures are performed on such spontaneous, baseline-subtracted population vectors of pyramidal activity, which we refer to as *representations*.

Finally, to identify the primary pyramidal neurons (i.e., those directly activated by the OB, without the need for recurrent excitation), we simulated again the first and last test days under the exact same conditions, but setting to zero all pyramidal-to-pyramidal synaptic efficacies. Secondary neurons for a given odor and day were then identified as those that showed over-baseline spiking activity in the original experiment, but were unresponsive after removing intracortical connections.

## Results: Quantitative comparison between model and experiments

**Representational drift in the PCx.** Using our model, we studied characteristics of RD systematically and compared our results with experimental measurements by Schoonover et al (6). First, we focused on the single-unit firing rate responses for each odor across days. As shown in Fig. 2a, we found the responses to the same odor became increasingly dissimilar over time. The squared Pearson-correlation ( $R^2$ ) decreases with time interval:  $R^2 = 0.94, 0.70, 0.56, 0.46, 0.35$  for within-day, 8-day, 16-day, 24-day, 32-day intervals, respectively, which quantitatively agrees with experimental results (6). The drift can also be measured by the average distance between a given odor representation on the first test day and the representation of the same odor on a later day as shown in Fig. 2b.

Next, we analyzed the angle between trial-averaged population vectors (corrected for within-day variability; see Methods) on different test days in our model and compared it to the experimental measurements. In Fig. 2c, we showed the accumulative distributions of the normalized angles between representations for the same odor but on different test days as well as the angle between representations of two different odors measured on the same day (gray line) for reference. It is clear from Fig. 2c that as the time interval in-

creases, the cumulative distributions shift to the right indicating an increase in the angle. However, even for the longest time interval of 32-days (red line in Fig. 2c), the same-odor angle is still smaller than the same-day different-odor angle (gray line). Quantitatively, the average angles for different interval times are in excellent agreement with experimental measurements (6) as shown in Fig. 2d (black symbols: simulations; gray symbols: experiments). Moreover, measures of the average drift rate per day (see Eq.(21) in Methods) resulted in a distribution with  $\bar{r} = 1.3^\circ \pm 0.4^\circ$  (Fig. 2e), which is in quantitative agreement with the experimental result (6):  $\bar{r}_{exp} = 1.3^\circ \pm 1.2^\circ$ . Pearson correlations between all trial-averaged population responses to a common odor were also computed across all possible pairs of test days (Fig. 2f), showing that the average pair-wise correlation decreased with the time span between representations (Fig. 2g) in agreement with experiments.

To rule out the possibility that the observed changes in odor-evoked responses originate from changes in overall population activity (for instance, the network becoming more reactive to stimuli), we studied the population-level statistics of the system. We found that despite the drifting response of individual neurons, the population-level statistics (see Methods section) remain stable across days. As shown in different panels in Fig. 2h, the fraction of responsive neurons (see also Fig. S.1c), population sparseness (Eq. (24)), lifetime sparseness (Eq. (25)), and within-day correlations (Eq. (16)) remain stable over the 32-day period, consistent with experimental observations (6).

The quantitative discrepancies with the experimental values may be caused by the particular choices of model parameters such as the size of the system, the sparsity of LOT connections, and the way we modeled the odors at the OB level. For example, in our model, odor responses involve on average a smaller fraction of the total PCx population (greater population sparseness), and the responsive neurons are specifically tuned to a small numbers of stimuli (greater lifetime sparseness; see Fig. S.1d in the SI). However, these quantitative differences do not affect the general conclusion regarding stability of the population-level statistics.

As expected, drift in cortical representations was manifested at the single-neuron level as observed in the experiments (6). In particular, pyramidal neurons fall into several categories in terms of their responses to the odors over time: (i) neurons that gained sensitivity to an odor (Fig. 2h and Fig. S.1f, unit #20; Fig. S.1g, units highlighted in blue); (ii) initially responsive neurons that eventually lost their responsiveness (Fig. 2h and Fig. S.1f, unit #998; Fig. S.1g, units highlighted in red); and (iii) neurons that showed a relatively stable response across all days (Fig. 2h and Fig. S.1f, unit #115). Quantitatively, only  $1.92 \pm 0.35\%$  of all considered pyramidal units showed a stable response (Wilcoxon rank-sum test,  $\alpha = 0.005$ ) across the full panel of odors (experimental value:  $2.5 \pm 0.5\%$  (6)). Similarly, the percentage of pyramidal units maintaining a stable response to a given odor was  $7.3 \pm 0.9\%$  (Fig. 2i), also in perfect agreement with the experimentally measured value ( $6.6 \pm 0.9\%$  (6)). Thus,

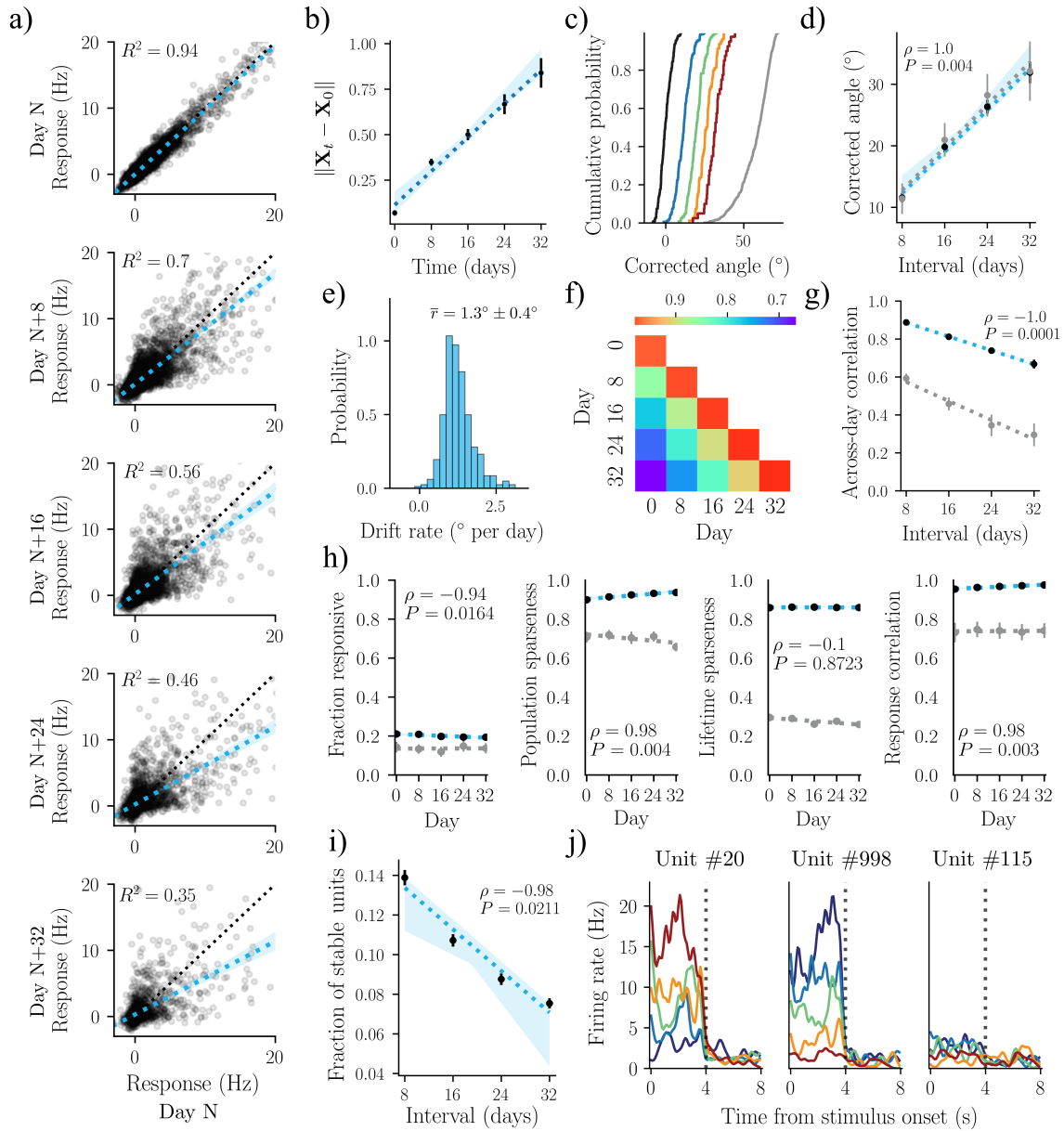


**Fig. 2. Odor representations drift despite invariant population statistics.** (a) Regression of firing rate responses within day (even vs odd trials, top panel) and across 8- to 32-days intervals for 500 randomly chosen odor-unit pairs. Black dashed line indicates identical response. (b) Euclidean distance between same-odor representations on first and later test days, averaged over odors and trials, and normalized by average within-day distance for different odor representations. (c) Cumulative probability distribution for the corrected angle between same-odor representations on a given day (black), across 8-, 16-, 24- and 32-day intervals (blue, green, yellow and red, respectively), and between different odors on the same day (gray). (d) Evolution of average corrected angle with interval between test days. (e) Histogram for the observed drift rate in degree angles per day. (f) Average population vector correlations for same-odor representations across days. (g) Average correlation decay against time interval between test days. (h) Population statistics, including, on each test day and from left to right: fraction of responsive neurons (Wilcoxon rank-sum test,  $\alpha = 0.005$ ); average population sparseness; average lifetime sparseness and average within-day correlations. (i) Fraction of pyramidal neurons that show a stable response to a given odor across the experiment, averaged over all odors. (j) Trial-averaged instantaneous firing rates for three pyramidal neurons in response to a given odor, measured on days 0 (purple), 8 (blue), 16 (green), 24 (yellow) and 32 (red). Dotted line marks the end of stimulus presentation. For all plots, when measures are reproduced from (6), experimental results (gray markers) are compared with our simulations (black markers). Error bars were computed as the standard deviation across  $n = 6$  realizations of the experiment (i.e., across mice in the experimental results and different initial conditions in the simulations). Shaded blue regions in linear regressions represent 95% confidence interval.

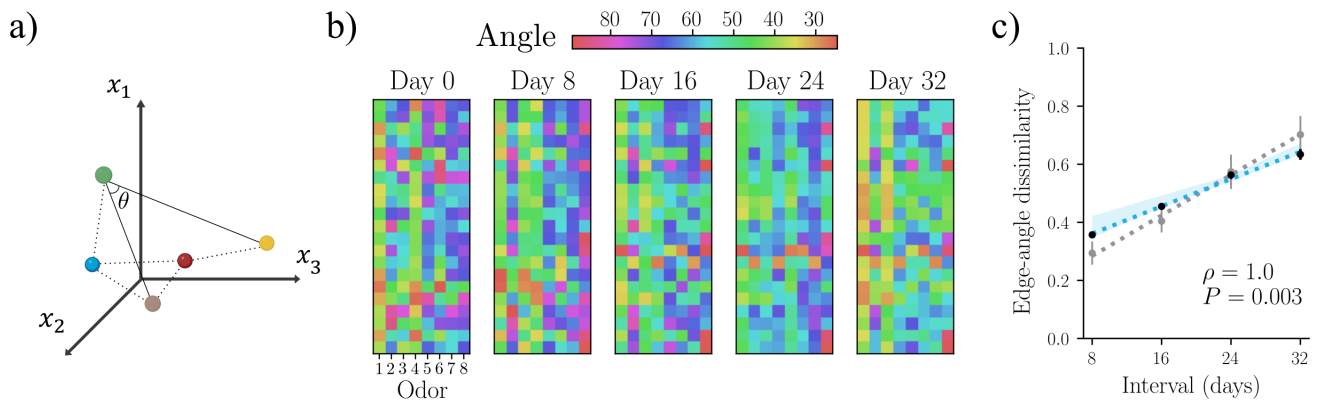


**Fig. 3. The geometry of odor representation manifolds changes with time.** (a) Schematic depiction of a hypothetical representation manifold geometry, marking one of the angles defined by the population vector responses to three different odors. (b) Edge-angle similarity matrices at test days. Note that for each odor/node there are 21 possible associated angles, which define the number of rows in the similarity matrix (c) Edge-angle corrected dissimilarity measure as a function of the time interval between test days ( $\rho$  and  $P$  denote the correlation coefficient and  $p$ -value for the linear regression). Error bars were computed as the standard deviation across  $n = 6$  realizations of the experiment (i.e., across mice in the experimental results and different initial conditions in the simulations).

in line with the experiments, our model induces progressive changes in the selectivity of units which accumulate over time across the duration of the experiment (Fig. S.1h).

From our model, we can also identify two types of pyramidal neurons responsive to a given odor: primary neurons, which are directly excited by the OB, and secondary neurons, which are recruited by the primary neurons through the recurrent connections. While the relative fraction of primary and secondary responsive units is stable across days (Fig. S.1e), we found that primary neurons are relatively more stable across the 32-day experiment than secondary ones (Fig. S.1i).

**Geometry of the representation space.** Despite the observed drift for individual odors, it has been suggested that the relative positions of different stimuli in the representational space may remain invariant (12). To test whether such an invariant geometry was present in our model, we computed the relative angles among odor representations following the same methodology as in (6). More specifically, for each individual day  $p$ , an odor similarity matrix  $A^p$  can be computed. As shown in Fig. 3b, each column corresponds to an individual odor (e.g., the green dot in Fig. 3a) and each row corresponds to a pair of other odors (e.g., the yellow and gray dots in Fig. 3a). Thus, each matrix element of  $A^p$  is defined as the cosine similarity angle  $\theta$  spanned by three odors in the representation space (see Methods for details).

As shown in Fig. 3b, the similarity matrices for different days change significantly with time, indicating the absence of a time-invariant geometrical structure in the odor representation space. As a way of quantifying this change in the geometry (relative position) of the representation space for different odors, we measured the *matrix dissimilarity* ( $\|A^{p,q}\|_F := \|A^p - A^q\|_F$ , where  $F$  stands for Frobenius norm) between any two test days  $p$  and  $q$  (see Methods). Fig. 3c shows the value of this quantity against the time interval between the considered similarity matrices. In agreement with experimental results (gray markers), changes in edge angles between encoded odor responses accumulate over time, indicating a lack of geometrical invariance in the representa-

tion space for the olfactory system.

However, although there is a lack of strict geometrical invariance with respect to the relative odor angles, the odors are always separable in the representational space. Furthermore, as we will describe in the Discussion section later in this paper, some geometrical properties of the odor representations such as the dimensionality of representations are found to be statistically invariant over time.

**The effects of stimulus-dependent plasticity.** So far, we only considered the effects of the slow stochastic synaptic dynamics for RD. We now turn our attention to the effects of learning on RD motivated by the insightful experiments by Schoonover et al. (6). Specifically, in (6) a cohort A of  $n = 5$  mice were presented with a panel of 4 odors daily across 16 days prior to the beginning of the experiment. Beginning on day 0, the same set of already “familiar” odors was still presented on a daily basis (Fig. 4a, cohort A, blue odors), but mice were also subject to a set of four “unfamiliar” odors at 8-day intervals (Fig. 4a, cohort A, red odors). Interestingly, a slower drift rate for the representations of familiar odors (i.e., those presented daily on the 16 days prior to the experiment) was observed when compared to the drift for the unfamiliar ones. Notably, a second cohort of mice in which the familiar odors were not presented daily after day 0, but at 8-day intervals instead (Fig. 4a, cohort B, blue odors), showed no statistically significant changes in the drift rate with respect to the unfamiliar ones. Taken together, these results suggest that “learned” representations of familiar stimuli would naturally drift as rapidly as representations of new inputs unless the familiar stimuli are presented with a higher frequency.

Here, we test whether our model, which incorporates the fast stimulus-dependent plasticity governed by the STDP learning rule, can explain these experimental observations by following the same protocols used in the experiments (Fig. 4a<sup>3</sup>) For our simulations of cohort A, we saw that

<sup>3</sup>In order to track the weight dynamics, we reduced the network size and adjusted the density and average weight of connections accordingly to keep

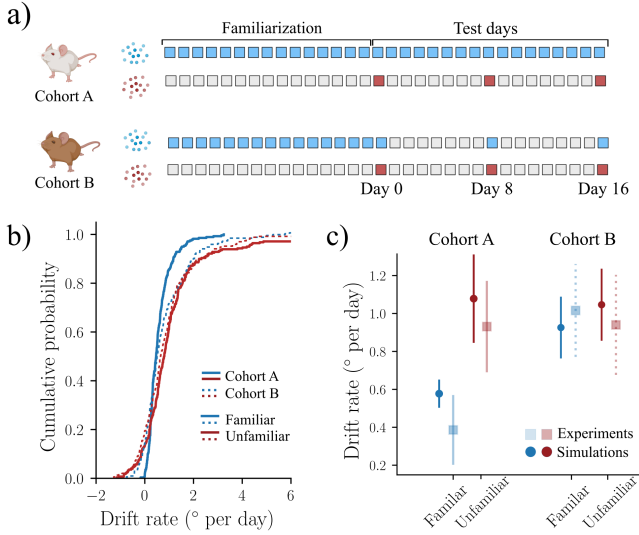


**Fig. 4. Representational drift depends on the frequency of stimulus presentation.** (a) Experimental setup to assess the dependence of the drift on the frequency of stimulus presentation, showing the two different cohorts of mice considered in the original experiment. (b) Cumulative probability distribution for the drift rate in each simulated “cohort” and across familiar and unfamiliar odors. (c) Mean drift rate (in degrees per day) across odors in each of the simulated experiments, with the experimental values from (6) plotted for comparison. For each condition, values were averaged over 8 odors and  $n = 5$  “mice” (i.e., different initial networks), with error bars representing a 95% CI.

angles between same-odor representations measured on different days are larger in the unfamiliar odor case than in the familiar odor case (Fig. 4b, see also Fig. S.2d in SI). Quantitatively, this translates into an average drift rate for the unfamiliar odor that is twice as fast ( $\bar{r}_{unf} = 1.1(0.9 - 1.3)^\circ$  per day), as compared to the case when in which familiar odors were presented daily ( $\bar{r}_{fam} = 0.58(0.64 - 0.53)^\circ$  per day), in excellent agreement with the experiments as shown in Fig. 4c. In the case of familiar odors presented every test day, we found that responses of individual neurons were more stable (Fig. S.2b), showing slowly decaying correlations (Fig. S.2c) and smaller average distances between across-days representations (Fig. S.2e).

We conducted additional simulations changing the interval between stimulus presentations from 1 to 8 days (thus interpolating between the conditions for familiar odors in cohort A and B). Our model results show that RD continuously decreased with the stimulus presentation frequency. While the reduction is minimal for the 8-day presentation interval, it increases to  $\sim 30 - 40\%$  for the 1-day presentation frequency (see Fig. 4c and Fig. S.2f in SI). We also verified that the model results were not due to the reduced system size, nor the particular new set of parameters (see Fig. S.2g in SI).

Verified by its agreement with experiments, our model can be used to gain insights about the underlying mechanism for how learning suppresses RD. By systematically probing the dynamics of the system, including the synaptic weights in our model, an intuitive picture of RD and the effects of learning emerged. As illustrated in Fig. 5a, through exposure to a particular odor, synaptic plasticity mechanisms lead to a learned representation,  $\mathcal{D}_0$ , of a given odor in the PCx across simulations computationally feasible (see Methods)

activity space. The representations of a particular odor are not unique – they span a low-dimensional sub-manifold in the full representation space as illustrated in Fig. 5a. During the long time interval,  $T$ , between odor presentations, neural activity wanders off the sub-manifold due to stochastic synaptic dynamics to a point  $\mathcal{D}_T$  away from it. However, the weight change induced by learning during presentation of the odor at time  $T \rightarrow T + \Delta t$  can drive the system back to another point,  $\mathcal{D}_{T+\Delta t}$ , on (or near) the representation sub-manifold. Thus, the odor-dependent learning effectively reduces RD by suppressing fluctuations away from the low-dimensional odor-specific sub-manifold, i.e.,  $\|\mathcal{D}_0 - \mathcal{D}_{T+\Delta t}\| < \|\mathcal{D}_0 - \mathcal{D}_T\|$  (see Fig. 5a).

To verify this intuitive picture, we measured the dynamics of relevant MTC-to-pyramidal weights in our model during an experiment where a particular familiar odor was presented every day after familiarization (Fig. 4a). As shown in Fig. 5b, odor presentation induces directed weight changes, i.e., changes with the same sign, while weights fluctuate randomly in-between test days.

To characterize the collective weight changes in the whole system, we projected the dynamics of non-zero LOT connections onto the first three principal components that are obtained by applying PCA to the recorded weights during odor presentation on the first day (Fig. 5c). As we can see, while the random multiplicative fluctuations caused by the GMR process push the weights in all directions, STDP-mediated changes can compensate the random drift, consistently across one of the principal component directions (see arrows in Fig. 5c).

Finally, to quantify the overall changes in weight space, we computed the normalized Euclidean distance with respect to the original set of weights using the first 10 principal components, which account for  $\sim 99\%$  of the total variance:

$$\|\Delta \mathbf{J}_{mtc}(t)\| = \frac{\|\mathbf{J}_{mtc}(t) - \mathbf{J}_{mtc}(0)\|}{\|\mathbf{J}_{mtc}(T) - \mathbf{J}_{mtc}(0)\|}, \quad (2)$$

where  $\mathbf{J}_{mtc}(t)$  is a 10-dimensional projection of the LOT weights at time  $t$ , and  $T$  represents the last time step after 9 simulated days. Fig. 5d shows that the Euclidean distance is reduced after each presentation of the stimulus (vertical dotted lines), which effectively decreases the rate at which drift takes place.

## Conclusions and Discussion

Understanding how information from the external world is encoded in cortical neuronal activity requires careful analysis of experimental data in combination with computational modeling based on realistic neural networks. Here, we focus on the olfactory cortex and the experimentally observed representational drift (RD) in the response of pyramidal cells, as reported by Schoonover *et al.* (6).

To understand the underlying mechanism for the observed RD phenomenon, we incorporate dynamics of synaptic plasticity in a realistic spiking neural network model of the mouse olfactory cortex. Our model reproduces all the main

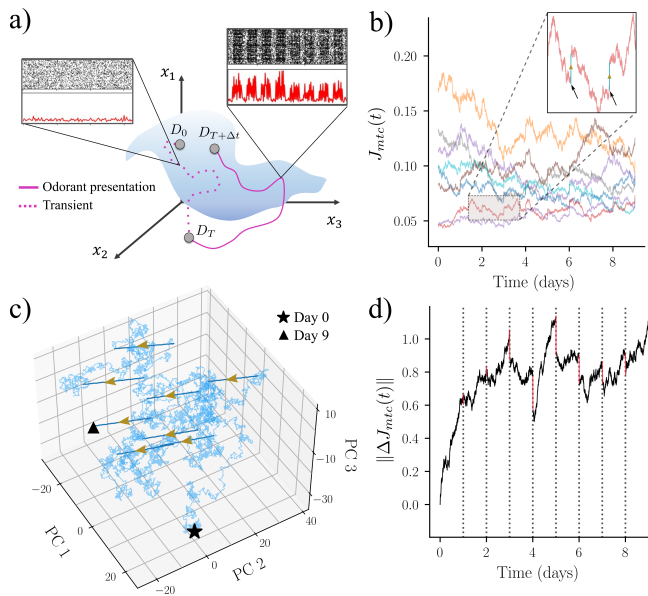


**Fig. 5. A mechanistic picture of learning-dependent drift.** (a) Schematic depiction for the evolution of an initial odor representation,  $D_0$ , to a new representation,  $D_{T+\Delta t}$ , reached after a long transient of length  $T$  and the presentation of the stimulus for a time span  $\Delta t \ll T$ . (b) Evolution of some weights during the simulated experiment with a familiar odor presented daily. Inset: close-up of a particular weight evolution, with black arrows pointing to the times of odor presentation. The large changes in weights during the odor presentation are highlighted by green arrowed lines. Weights were sampled every  $\Delta t = 60\text{s}$  during transient, and  $\Delta t = 50\text{ms}$  during stimulus presentation. (c) Projection of the weights dynamics into the first three principal components resulting from applying PCA during the presentation of the odor on the first day. Slow random fluctuations during inter-tests transients (light blue) are followed by fast, directed changes during odor presentation (dark blue). Arrows indicate time direction during the experiment. (d) Normalized distance, in the projection space spanned by the first 10 principal components, between the initial weight configuration and the weights at time  $t$ . Dotted vertical lines mark the time of odor presentation, coinciding with sharp drops in the measured distance (highlighted in red).

experimental findings reported in (6) quantitatively. More importantly, it elucidates a general mechanism underlying RD and the effects of learning, which may be applicable to other brain regions that exhibit RD. In what follows, we discuss our main findings and possible future directions.

**Slow drift by stochastic weight variations.** Synapses in the cortex are highly dynamic and can change in time regardless of the existence or absence of a stimulus, with synaptic efficiencies spontaneously fluctuating over a long timescale of days without altering their overall statistics. As a result of this stochastic process, the response of cortical pyramidal cells to a given odor signal—constituting the cortical representation of the odor—drifts slowly, while the statistical properties of the representation remain stable over time. Our study finds that the spontaneous weight fluctuations are best described by an Ornstein-Uhlenbeck process with multiplicative noise (Eq. 1), also known as the geometric mean reversion (GMR) process. Our realistic network model, with weight dynamics governed by the GMR process, not only quantitatively reproduces all experimental results on RD in the piriform cortex (6) but also results in a log-normal distribution of the weights in steady state, consistent with empirical observations across brain regions (33, 35).

**Learning suppresses representational drift.** In the presence of odors that induce strong responses in the olfactory system, significant changes in synaptic weights can occur via local learning rules, such as spike-timing-dependent plasticity (STDP), during the relatively short time window of odor presentation. Rather than being random, these systematic weight changes drive the system towards a lower-dimensional sub-manifold in the representational space, as illustrated in Fig. 5a, effectively compensating for the deviations induced by the spontaneous noisy drift. Consequently, when the frequency of odor presentation is increased, drift rate is reduced, as illustrated in our model (Fig. 4 and Fig. S.2f) and in agreement with experimental observations (6). Notably, this mechanism of drift reduction requires the existence of a “learned” representation induced by previous exposure of the animal to a given odor (referred to as the “familiarization” phase in the experiments (6)).

**Absence of an invariant geometry.** Consistent with the experiments by Schoonover et al (6), our model shows that the geometry of the drifting representation manifold is not invariant across time. Specifically, the relative angles between pairs of odor-specific responses in the representational manifold do not remain constant over time, both in the original experiments and our model. This observation contrasts with the findings in a recent study by Qin *et al.* (12), who developed a model to explain RD with Hebbian/anti-Hebbian networks. In their work, the learning dynamics aims to minimize the mismatch between the similarity of pairs of inputs and corresponding pairs of outputs, resulting in a coordinated drift that preserves the manifold geometry.

On the functional side, we contend that geometric considerations are crucial when the inputs or stimuli to be encoded have a well-defined geometry. This is certainly the case for spatial locations or motion orientations encoded in the hippocampus, which is one of the focuses of study in (12). In these scenarios, the representation manifold must reflect the actual spatial organization of stimuli, and this objective is best achieved if the representation manifold preserves geometric properties such as relative angles. Instead, in our modeling study of the piriform cortex presented here, the set of possible stimuli, i.e., odors, lacks any specific organization. As long as they are separable, the relative angles between representations of different odors do not seem to encode useful information; in particular, the similarity between two different odors may not be directly related to the scalar product (an Euclidean distance measure) in either the input space or the representational space.

Indeed, studies by the Sharpee group (36, 37) have proposed that the olfactory space is hyperbolic rather than Euclidean, which could reflect a hierarchical organization in the odor space (38). Therefore, in future extensions of our work, we will seek to replace randomly organized odors with hierarchically structured ones to analyze whether the resulting representation manifold exhibits hyperbolic geometry (by keeping, e.g., hyperbolic inner products and angles fixed).



### Invariant properties of the representation manifold.

Even though the geometry of the representation manifold is not invariant, certain aspects of the representation remain preserved. In particular, the covariance matrix for pyramidal neurons presents an underlying block structure that is preserved over time. While the identity of the neurons participating in each block changes across days, the number of strongly correlated blocks remains constant and matches approximately the number of odors presented to the system (Fig. S.1k). Notably, a similar phenomenology was found by Kossio *et al.* in a work that studied RD using an associative memory computational model (11). In particular, the authors proposed a mechanism by which STDP and homeostasis could maintain a constant representational structure despite the existence of drifting neural assemblies. However, unlike in our model, the emergence of this neuronal assemblies required a mechanism to generate symmetric connectivity matrices, which also encoded the block structure within their architecture (11).

Besides the invariant representational structure in correlations, a principal component analysis of the pyramidal activity in response to the presented stimuli shows that the effective dimensionality of the representation manifold remains constant and is close to the number of encoded odors (Fig.S.1l). We speculate that for hierarchically structured odor stimuli, the covariance matrix should exhibit a nested hierarchical block structure and, consequently, could be describable by an invariant hyperbolic geometry (37, 38).

**Beyond the olfactory cortex: shedding light on the slow vs fast drift conundrum.** Experimental studies have shown the emergence of drifting representations on very long timescales of days or weeks in diverse brain regions (6, 7, 39, 40). However, in a recent work by Khatib *et al.* (41), where mice were trained to navigate a familiar maze, it was found that for a set amount of time, the more frequently the mice explored the environment, the greater the degree of drift observed in the neural representation of the spatial location in dorsal CA1 of the mouse hippocampus, a result that has been recently addressed computationally (9).

We would like to point out that, contrary to what it might seem, this result is not at odds with the empirical observation made by Schoonover *et al.* regarding drift slowing down with the frequency of stimulus presentation. Indeed, for the experiments in (41), drift was measured between population neuron activities recorded with a time difference of  $\sim 3$  hours. Following our hypotheses, at these shorter timescales changes in representations are not really the result of a *drift* as caused by the noisy weight dynamics, but actually originate from what we called a *learning force* through STDP effects while mice were traversing the familiar environment. This conclusion is indeed supported by the findings of two other experimental papers in the dorsal CA1 region of the mouse hippocampus (42), and the telencephalic area Dp of the adult zebra fish (30), which we discuss below.

In the Geva *et al.* (42) study, the authors carried out an experiment similar to the one in (41), but sampled neural activity for a time-span of 3 weeks. Within such much-longer

recordings, they were able to confirm the existence of time-dependent drift that mostly affected changes in activity rates, and an experience-dependent drift that affected neural tuning curves. In another study, Jacobson *et al.* (30) showed that the substantial variability observed in zebra-fish Dp neural activity for a given odor across trials, which they called *representation shift*, was severely reduced by an NMDA receptor antagonist, implying that these modifications were indeed experience-dependent.

All these findings suggest that representational drift, as measured between population responses to the same input across days, is caused by two contributing mechanisms: (i) an actual random drift, which we hypothesize stems from noisy multiplicative weight dynamics; and (ii) a learning force, induced by STDP on a shorter timescale when the represented external input is experienced (e.g., positions in space (40–42)) or presented (e.g., odors (6, 30) or visual stimuli (10, 43)). While the first mechanism always leads to random drift, the effects of learning on RD depend on the timescale of measuring representational drift. On longer timescales (of days or weeks), learning leads to suppression of RD as it effectively reduces the effects of random drift. However, for shorter measurement timescales, learning can increase the measured drift as it drives the system deterministically towards its learned representation sub-manifold. The role of learning and its dependence on the measurement time scale are demonstrated analytically in a toy model in SI (Supplementary Note 2).

Although the main focus of this article was on reproducing and explaining through a biologically realistic computational model the experimental findings of Schoonover *et al.* in (6), preliminary results suggest that our proposed mechanisms for drift are also in very good agreement with experimental observations in other regions, such as a non-trivial alignment of drift changes with the directions of noise variance in the mouse posterior parietal cortex (44) (see SI, Supplementary Note 3).

## Methods

**OB dynamics.** In our simulations, and following the model by Stern *et al.* (22), all MTCs belonging to glomerulus  $i$  share a specific onset latency time,  $\tilde{\tau}_i^o$ , which is different for each odor,  $o$ . In particular, these latency times were randomly drawn from a uniform distribution such that only an average 10% of all MTCs become responsive to a given odor within the inhalation period (i.e.,  $\tilde{\tau}_i^o < \tau_{inh}$ ).

Thus, while MTCs have a baseline firing rate at 1.5Hz, if glomerulus  $i$  is activated during inhalation of a given odor,  $o$ , the instantaneous firing rate of all units belonging to this glomerulus jumps to 100Hz at time  $\tilde{\tau}_i^o$ , and then decays exponentially to the baseline rate with a characteristic time constant  $\tau_{mTC} = 50\text{ms}$ .

For all simulations, one trial of odor presentation lasted 8 respiration cycles, each consisting of a 200ms inhalation period, followed by a 300ms exhalation period. Figs. 1-3, Fig. S.1 and Fig. S.2g:  $N_{MTC} = 2250$  and  $n_{glom} = 90$ , so that each glomerulus has 25 associated MTCs.

For simulations involving familiar and unfamiliar odors (Figs. 4-5 and Fig. S.2a-f), we set  $N_{MTC} = 300$  and  $n_{glom} = 60$ , so that each glomerulus has 5 associated MTCs. In this latter case and to avoid undesired cross-stimuli effects due to the network limited size (i.e., the familiarization process to one odor significantly affecting the representation of a second odor), we conducted simulations presenting one odor at a time, resetting to the exact same initial conditions for the network at the beginning of each experiment.

**PCx dynamics.** The below-threshold voltage dynamics of pyramidal neurons and FBINs take the general form of a LIF equation:

$$\tau_m \frac{dV_i}{dt} = -(V_i(t) - V_{rest}) + I_i^{tot}(t), \quad (3)$$

where  $I_i^{tot}(t) = I_i^{exc}(t) + I_i^{inh}(t)$  is the sum of all incoming excitatory and inhibitory currents to neuron  $i$ ,  $\tau_m = 15\text{ms}$  is the membrane characteristic time scale and  $V_{rest} = -65\text{mV}$  is the resting potential. In the following equations,  $J_{ij}^{XY}$  denote the synaptic efficiencies between presynaptic neuron  $j$  belonging to population  $X$  and postsynaptic neuron  $i$  belonging to population  $Y$  (m:MTC, p:pyramidal, f:FFIN, fb:FBIN). Defining  $\Lambda_j = \sum_f \delta(t - t_j^f)$  as the train of spikes fired by neuron  $j$ , one can write for pyramidal units:

$$\tau_{exc} \frac{dI_i^{exc}}{dt} = -I_i^{exc} + \sum_{j=1}^{N_{MTC}} J_{ij}^{mp} \Lambda_j + \sum_{j=1}^{N_{PYR}} J_{ij}^{pp} \Lambda_j, \quad (4)$$

$$\tau_{inh} \frac{dI_i^{inh}}{dt} = -I_i^{inh} + \sum_{j=1}^{N_{FBIN}} J_{ij}^{fbp} \Lambda_j + \sum_{j=1}^{N_{FFIN}} J_{ij}^{fp} \Lambda_j. \quad (5)$$

Similarly for FBINs:

$$\tau_{exc} \frac{dI_i^{exc}}{dt} = -I_i^{exc} + \sum_{j=1}^{N_{PYR}} J_{ij}^{pfb} \Lambda_j, \quad (6)$$

$$\tau_{inh} \frac{dI_i^{inh}}{dt} = -I_i^{inh} + \sum_{j=1}^{N_{FBIN}} J_{ij}^{fbfb} \Lambda_j, \quad (7)$$

whereas for FFINs:

$$\tau_{exc} \frac{dI_i^{exc}}{dt} = -I_i^{exc} + \sum_{j=1}^{N_{MTC}} J_{ij}^{mf} \Lambda_j, \quad (8)$$

$$\tau_{inh} \frac{dI_i^{inh}}{dt} = -I_i^{inh} + \sum_{j=1}^{N_{FFIN}} J_{ij}^{ff} \Lambda_j. \quad (9)$$

In the above equations,  $\tau_{exc} = 20\text{ms}$  and  $\tau_{inh} = 20\text{ms}$  represent the characteristic decay time for the excitatory and inhibitory input currents. Notice that, for simplicity, we reabsorbed the membrane conductance  $g_m$  into the definition of input current, so that all currents and synaptic efficiencies are expressed in units of voltage. Moreover, while in the original work by Stern *et al.* all synaptic weights connecting the

same type of neurons were set to a common value (22), in our model, weights were randomly drawn from a lognormal probability distribution with a given average  $\langle J^* \rangle$  and standard deviation  $\sigma = \langle J^* \rangle / 2$ .

Once a neuron reaches its firing threshold,  $V_{th} = -50\text{mV}$ , its membrane potential is reset and clamped to a value  $V_{reset} = -65\text{mV}$  for a refractory period,  $\tau_{ref} = 1\text{ms}$ , before it can evolve again according to Eq. (3). We did not allow membrane potentials to decrease below a minimum value,  $V_{min} = -75\text{mV}$ . For all types of neurons, the dynamical equation was integrated using a 4th-order Runge-Kutta algorithm with a time step  $\Delta t = 0.0005\text{s}$ .

For Figs. 1-3, Fig. S.1 and Fig. S.2g, weight distribution averages and density of connections were chosen to enforce the same excitatory and inhibitory currents to each population as in (22):  $\langle J_{mp}^* \rangle = \langle J_{mf}^* \rangle = 4\text{mV}$ ,  $\langle J_{fp}^* \rangle = \langle J_{ff}^* \rangle = 3\text{mV}$ ,  $\langle J_{pp}^* \rangle = 1\text{mV}$ ,  $\langle J_{pfb}^* \rangle = 4\text{mV}$ ,  $\langle J_{fbp}^* \rangle = \langle J_{fbfb}^* \rangle = 3\text{mV}$ . Density of connections:  $p_{mp} = p_{mf} = 0.022$ ,  $p_{fp} = p_{ff} = 0.4$ ,  $p_{pp} = p_{pfb} = p_{fbp} = 0.1$ ,  $p_{fbfb} = 0.065$ .

For experiments involving familiar and unfamiliar odors (Figs. 4-5 and Fig. S.2a-f), we reduced the number of neurons in the piriform cortex to  $N_{PYR} = 100$  and  $N_{FBIN} = 20$ , limiting the inhibition of pyramidal cell activity to FBINs only, thus disregarding the effect of FFINs, which have been shown to simply modulate the amplitude but not the shape of pyramidal responses (22). For the average weights:  $\langle J_{mp}^* \rangle = 3\text{mV}$ ,  $\langle J_{pp}^* \rangle = 5\text{mV}$ ,  $\langle J_{pfb}^* \rangle = \langle J_{fbp}^* \rangle = \langle J_{fbfb}^* \rangle = 20\text{mV}$ . Density of connections:  $p_{mp} = 0.025$ ,  $p_{pp} = 0.1$ ,  $p_{fbp} = p_{pfb} = p_{fbfb} = 0.4$ .

**Weight dynamics.** There are two different synaptic plasticity in our model, i.e., the slow stochastic weight changes described by the geometric mean-reversion process and the fast weight dynamics due to learning.

**The geometric mean-reversion process.** The dynamics of synaptic weights in both, mitral-to-pyramidal and pyramidal-to-pyramidal connections, were modeled as a geometric mean-reversion process:

$$\dot{J}_k = \omega(\mu - J_k(t)) + \sigma J_k(t) \xi_k(t), \quad (10)$$

where  $k$  indexes all non-zero synaptic efficiencies in the weight matrix,  $\omega$  and  $\sigma$  are constants for the drift and diffusion terms,  $\mu = \langle J^* \rangle$  is the average non-zero weight in the initial Gaussian distribution (and will be, likewise, the average weight of the resulting stationary lognormal distribution) and  $\xi(t)$  is a zero-mean Gaussian noise, such that  $\langle \xi_k(t) \rangle = 0$  and  $\langle \xi_i(t) \xi_j(t') \rangle = \delta_{ij} \delta(t - t')$ . In all simulations, we chose  $\omega = 5 \times 10^{-7}$  and  $\sigma = 4.5 \times 10^{-4}$ . Before the beginning of each experiment, we also let the weights evolve for 32 days under the above rule to ensure that a stationary lognormal probability distribution had been reached (see Fig. 1e).

**Spike-timing dependent plasticity.** It has been experimentally observed that long-term potentiation (LTP) and long-term depression (LTD) of synaptic weights depend on the exact timing of the pre- and postsynaptic spikes (45-47). LTP is typically induced when the presynaptic spike precedes the post-

synaptic one by an interval of 10 to 20ms, whereas LTD occurs if the order of spikes is reversed (see Fig.1a, bottom). This mechanism of STDP has been largely studied from a theoretical point of view (34, 48–51) and many models have been proposed to investigate its functional implications (see (52) and (53) for reviews on the topic).

Mathematically speaking, the change in the synaptic weight induced by pre- and postsynaptic spikes at time  $t_{pre}$  and  $t_{post}$ , respectively, can be written as:

$$\Delta J = \Gamma(J; t_{post} - t_{pre}) \quad (11)$$

where  $\Gamma(w; t_{post} - t_{pre})$  is the plasticity window, which can lead to potentiation (LTP) or depression (LTD) depending on the relative timing of the spikes,  $\Delta t^* = t_{post} - t_{pre}$ :

$$\Gamma(J; \Delta t^*) = \begin{cases} f_+(J) \exp\left(-\frac{|\Delta t^*|}{\tau_+}\right), & \text{if } t_{pre} < t_{post} \\ f_-(J) \exp\left(-\frac{|\Delta t^*|}{\tau_-}\right), & \text{if } t_{pre} > t_{post}. \end{cases} \quad (12)$$

Within the above expression different choices of the scaling functions for potentiation,  $f_+(w)$ , and depression,  $f_-(w)$ , can give rise to different models of STDP (53). Here we use a *multiplicative* STDP, as originally proposed in (34) —on the basis of experimental observations in (54)—, for which the LTP and LTD scaling functions read:

$$f_+(J) = a_+, \quad (13)$$

$$f_-(J) = -a_- J, \quad (14)$$

for some constant values  $a_+$  and  $a_-$ . All simulations were ran using  $\tau_+ = 17\text{ms}$  and  $\tau_- = 34\text{ms}$  for the LTP and LTD windows, respectively, and  $a_+ = 0.0005\langle J^* \rangle$ . The gain factor for LTD,  $a_-$ , was chosen in each case so that the average weight of the stationary distribution under the STDP rule ( $\langle J^{st} \rangle = (a_+ \tau_+) / (a_- \tau_-)$ , see (48)), matches the average weight,  $\langle J^* \rangle$ , of the expected lognormal distribution under the GMR process.

**Measures of drifting representations.** For each day  $d$ , odor  $o$  and trial  $m$ , the representation of an odor,  $\mathbf{x}_{d,o,m}$ , was computed by averaging pyramidal responses in time across four 2s-windows after odor onset, then concatenating the corresponding vectors so that  $\mathbf{x}_{d,o,m} \in \mathbb{R}^{4N_{PYR}}$ . For each neuron (i.e., element in  $\mathbf{x}_{d,o,m}$ ) its average baseline spontaneous rate, computed as the average rate across all days during the transient periods, was subtracted in all cases before computing any drift-related quantity.

Correlation between same-odor representations at days  $p$  and  $q$ , with  $p \neq q$ , was defined as the average across odors of the Pearson's correlation coefficient between trial-averaged population vectors at the corresponding days:

$$c_{p,q} = \frac{1}{n_{odors}} \sum_{o=1}^{n_{odors}} \frac{\langle (\mathbf{x}_{p,o} - \bar{\mathbf{x}}_{p,o})(\mathbf{x}_{q,o} - \bar{\mathbf{x}}_{q,o}) \rangle}{\sigma_{\mathbf{x}_{p,o}} \sigma_{\mathbf{x}_{q,o}}} \quad (15)$$

where  $\mathbf{x}_{p,o} = M^{-1} \sum_{m=1}^M \mathbf{x}_{p,o,m}$  is the trial-averaged population response to odor  $o$  on day  $p$ , and  $\bar{\mathbf{x}}_{p,o}$  and  $\sigma_{\mathbf{x}_{p,o}}$  define its mean and standard deviation, respectively.

Trivially, one can then define within-day correlations between odor responses by averaging population vectors across even and odd trials separately:

$$c_p = \frac{1}{n_{odors}} \sum_{o=1}^{n_{odors}} \frac{\langle (\mathbf{x}_{p,o}^{even} - \bar{\mathbf{x}}_{p,o}^{even})(\mathbf{x}_{p,o}^{odd} - \bar{\mathbf{x}}_{p,o}^{odd}) \rangle}{\sigma_{\mathbf{x}_{p,o}^{even}} \sigma_{\mathbf{x}_{p,o}^{odd}}}, \quad (16)$$

where  $\mathbf{x}_{p,o}^{even}$  ( $\mathbf{x}_{p,o}^{odd}$ ) is the population response to odor  $o$  on day  $p$  averaged over all even (odd) trials.

On the other hand, the average correlation between same-odor responses separated by a time interval of  $\Delta$ -days, is:

$$\bar{c}_\Delta = \frac{1}{n_\Delta} \sum_{p,q: |p-q|=\Delta} c_{p,q}, \quad (17)$$

where  $n_\Delta$  is the number of pairs of test days separated by a time interval  $\Delta$ .

Similarly, the average angle between a pair of population vectors representing the same odor at days  $p$  and  $q$  can be written as:

$$\theta_{p,q} = \frac{1}{n_\Delta} \sum_{o=1}^{n_{odors}} \theta_{p,q}^o = \frac{1}{n_{odors}} \sum_{o=1}^{n_{odors}} \cos^{-1} \left( \frac{\mathbf{x}_{p,o} \cdot \mathbf{x}_{q,o}}{\|\mathbf{x}_{p,o}\| \|\mathbf{x}_{q,o}\|} \right). \quad (18)$$

and the average within-day angle at each day  $p$  is defined as:

$$\theta_p = \frac{1}{n_{odors}} \sum_{o=1}^{n_{odors}} \cos^{-1} \frac{\mathbf{x}_{p,o}^{even} \cdot \mathbf{x}_{p,o}^{odd}}{\|\mathbf{x}_{p,o}^{even}\| \|\mathbf{x}_{p,o}^{odd}\|}. \quad (19)$$

To correct for within-day variability in the angle between representations of the same odor, we followed (6) and computed the average within-day angle,  $\bar{\theta} = \frac{1}{n_{days}} \sum_p \theta_p$ , between same-odor, same-day population responses. Thus, the average corrected angle between any two representations measured on tests separated by  $\Delta$ -days was finally computed as:

$$\bar{\theta}_\Delta = n_\Delta^{-1} \sum_{p,q: |p-q|=\Delta} (\theta_{p,q} - \bar{\theta}). \quad (20)$$

Using the above quantity, it is possible to measure the rate of drift (in angles per day and corrected for within-day fluctuations) as:

$$\bar{r} = \left\langle \frac{\bar{\theta}_\Delta}{\Delta} \right\rangle_\Delta, \quad (21)$$

where the average is taken across all possible time intervals,  $\Delta$ , between any pair of test days.

**Measures of drifting geometry.** Matrix dissimilarity between days  $p$  and  $q$  was taken as:

$$\|A^{p,q}\|_F := \|A^p - A^q\|_F = \sqrt{\sum_{k=1}^M \sum_{i=1}^{n_{odors}} |a_{k,i}^p - a_{k,i}^q|^2}, \quad (22)$$

where  $\|A^{p,q}\|_F = 0$  for identical matrices. Given the above measure, a corrected matrix dissimilarity was computed as:

$$\|\hat{A}^{p,q}\|_F := \frac{\|A^{p,q}\|_F - \overline{\|A^w\|_F}}{\|A^s\|_F - \overline{\|A^w\|_F}}, \quad (23)$$

where  $\overline{\|A^w\|_F} := (1/n_{days}) \sum_{p=1}^{n_{days}} \|A_{odd}^p - A_{even}^p\|_F$  is the mean across all days of the within-day Frobenius norm between similarity matrices computed in odd and even trials, and  $\|A^s\|_F$  is the Frobenius norm between similarity matrices measured on the first and last day of the experiment after odors shuffling. In this way,  $\|\hat{A}^{p,q}\|_F$  is (on average) bounded between zero, for angle drifts on the order of intra-day fluctuations, and one, for the shuffled case.

**Population statistics.** To identify responsive units, on each day and for each odor a Wilcoxon rank-sum test (55) was performed between the spike count during the 4 seconds before stimulus onset on all trials and the spike count on all trials during the odor presentation, using a significance level of  $\alpha = 0.005$ . On each day, the number of responsive neurons was averaged over all presented stimuli and normalized by population size to compute the average fraction of responsive neurons (see Fig. 2e (left panel)).

Given spontaneous baseline-subtracted responses,  $r_{j,o}$ , for each unit,  $j$ , to a given odor,  $o$ , average population sparseness was defined as:

$$S_p = \frac{N-1}{n_{odors}N} \sum_{o=1}^{n_{odors}} \left( 1 - \frac{\left( N^{-1} \sum_{j=1}^N r_{j,o} \right)^2}{N^{-1} \sum_{j=1}^N r_{j,o}^2} \right), \quad (24)$$

whereas the average lifetime sparseness across all units was given by:

$$S_{lt} = \frac{n_{odors}-1}{n_{odors}N} \sum_{j=1}^N \left( 1 - \frac{\left( n_{odors}^{-1} \sum_{o=1}^{n_{odors}} r_{j,o} \right)^2}{n_{odors}^{-1} \sum_{o=1}^{n_{odors}} r_{j,o}^2} \right). \quad (25)$$

#### ACKNOWLEDGEMENTS

This work has been supported by Grant No. PID2023-149174NB-I00 financed by MICIU/AEI/10.13039/501100011033 and EDRF/EU funds, as well as by PID2020-113681GB-I00, MICIU/AEI/10.13039/501100011033.

## Bibliography

- SueYeon Chung and L. F. Abbott. Neural population geometry: An approach for understanding biological and artificial neural networks. *Current Opinion in Neurobiology*, 70:137–144, October 2021. ISSN 0959-4388. doi: 10.1016/j.conb.2021.10.010.
- Carsen Stringer, Marius Pachitariu, Nicholas Steinmetz, Matteo Carandini, and Kenneth D Harris. High-dimensional geometry of population responses in visual cortex. *Nature*, 571(7765):361–365, 2019.
- Jason Mantley, Sihao Lu, Kevin Barber, Jeffrey Demas, Hyewon Kim, David Meyer, Francisca Martínez Traub, and Alipasha Vaziri. Simultaneous, cortex-wide dynamics of up to 1 million neurons reveal unbounded scaling of dimensionality with neuron number. *Neuron*, 112(10):1694–1709, 2024.
- Laurence F Abbott and Terrence Joseph Sejnowski. *Neural codes and distributed representations: foundations of neural computation*. MIT Press, 1999.
- Rafael Yuste. From the neuron doctrine to neural networks. *Nature reviews neuroscience*, 16(8):487–497, 2015.
- Carl E. Schoonover, Sarah N. Ohashi, Richard Axel, and Andrew J. P. Fink. Representational drift in primary olfactory cortex. *Nature*, 594(7864):541–546, June 2021. ISSN 1476-4687. doi: 10.1038/s41586-021-03628-7. Bandiera\_abtest: a Cg\_type: Nature Research Journals Number: 7864 Primary\_atype: Research Publisher: Nature Publishing Group Subject\_term: Cortex;Olfactory cortex;Sensory processing Subject\_term\_id: cortex;olfactory-cortex;sensory-processing.
- Laura N. Driscoll, Noah L. Pettit, Matthias Minderer, Selmaan N. Chettih, and Christopher D. Harvey. Dynamic Reorganization of Neuronal Activity Patterns in Parietal Cortex. *Cell*, 170(5):986–999.e16, August 2017. ISSN 0092-8674, 1097-4172. doi: 10.1016/j.cell.2017.07.021. Publisher: Elsevier.
- Dorgham Khatib, Aviv Ratzon, Mariell Sellevoll, Omri Barak, Genela Morris, and Dori Derdikman. Experience, not time, determines representational drift in the hippocampus, August 2022. Pages: 2022.08.31.506041 Section: New Results.

- Aviv Ratzon, Dori Derdikman, and Omri Barak. Representational drift as a result of implicit regularization. *eLife*, 12, April 2024. doi: 10.7554/eLife.90069.2. Publisher: eLife Sciences Publications Limited.
- Tyler D. Marks and Michael J. Goard. Stimulus-dependent representational drift in primary visual cortex. *Nature Communications*, 12(1):5169, August 2021. ISSN 2041-1723. doi: 10.1038/s41467-021-25436-3. Bandiera\_abtest: a Cc\_license\_type: cc-by Cg\_type: Nature Research Journals Number: 1 Primary\_atype: Research Publisher: Nature Publishing Group Subject\_term: Neural circuits;Sensory processing Subject\_term\_id: neural-circuit;sensory-processing.
- Yaroslav Felipe Kalle Kossio, Sven Goedeke, Christian Klos, and Raoul-Martín Memmesheimer. Drifting assemblies for persistent memory: Neuron transitions and unsupervised compensation. *Proceedings of the National Academy of Sciences*, 118(46), November 2021. ISSN 0027-8424, 1091-6490. doi: 10.1073/pnas.2023832118. Publisher: National Academy of Sciences Section: Biological Sciences.
- Shanshan Qin, Shiva Farashahi, David Lipschutz, Anirvan M. Sengupta, Dmitri B. Chklovskii, and Cengiz Pehlevan. Coordinated drift of receptive fields in Hebbian/anti-Hebbian network models during noisy representation learning. *Nature Neuroscience*, 26(2):339–349, February 2023. ISSN 1546-1726. doi: 10.1038/s41593-022-01225-z. Number: 2 Publisher: Nature Publishing Group.
- Michael E. Rule and Timothy O’Leary. Self-healing codes: How stable neural populations can track continually reconfiguring neural representations. *Proceedings of the National Academy of Sciences*, 119(7):e2106692119, February 2022. doi: 10.1073/pnas.2106692119. Publisher: Proceedings of the National Academy of Sciences.
- Kyle Aitken, Marina Garrett, Shawn Olsen, and Stefan Mihalas. The geometry of representational drift in natural and artificial neural networks. *PLOS Computational Biology*, 18(11):e1010716, November 2022. ISSN 1553-7358. doi: 10.1371/journal.pcbi.1010716. Publisher: Public Library of Science.
- Geoffroy Delamare, Yosif Zaki, Denise J. Cai, and Claudia Clopath. Drift of neural ensembles driven by slow fluctuations of intrinsic excitability. *eLife*, 12, December 2023. doi: 10.7554/eLife.88053.2. Publisher: eLife Sciences Publications Limited.
- Robin M Blazing and Kevin M Franks. Odor coding in piriform cortex: mechanistic insights into distributed coding. *Current Opinion in Neurobiology*, 64:96–102, October 2020. ISSN 0959-4388. doi: 10.1016/j.conb.2020.03.001.
- L. Buck and R. Axel. A novel multigene family may encode odorant receptors: a molecular basis for odor recognition. *Cell*, 65(1):175–187, April 1991. ISSN 0092-8674. doi: 10.1016/0092-8674(91)90418-x.
- Bettina Malnic, Junzo Hirono, Takaaki Sato, and Linda B. Buck. Combinatorial Receptor Codes for Odors. *Cell*, 96(5):713–723, March 1999. ISSN 0092-8674, 1097-4172. doi: 10.1016/S0092-8674(00)80581-4. Publisher: Elsevier.
- Yue Jiang, Naihua Natalie Gong, Xiaoyang Serene Hu, Mengjue Jessica Ni, Radhika Pasi, and Hiroaki Matsunami. Molecular profiling of activated olfactory neurons identifies odorant receptors for odors in vivo. *Nature Neuroscience*, 18(10):1446–1454, October 2015. ISSN 1546-1726. doi: 10.1038/nn.4104. Number: 10 Publisher: Nature Publishing Group.
- Peter Mombaerts, Fan Wang, Catherine Dulac, Steve K. Chao, Adriana Nemes, Monica Mendelsohn, James Edmondson, and Richard Axel. Visualizing an Olfactory Sensory Map. *Cell*, 87(4):675–686, November 1996. ISSN 0092-8674, 1097-4172. doi: 10.1016/S0092-8674(00)81387-2. Publisher: Elsevier.
- Norbert Hálasz and Charles A. Greer. Terminal arborizations of olfactory nerve fibers in the glomeruli of the olfactory bulb. *Journal of Comparative Neurology*, 337(2):307–316, 1993. ISSN 1096-9861. doi: 10.1002/cne.903370211. eprint: https://onlinelibrary.wiley.com/doi/pdf/10.1002/cne.903370211.
- Merav Stern, Kevin A Bolding, LF Abbott, and Kevin M Franks. A transformation from temporal to ensemble coding in a model of piriform cortex. *eLife*, 7:e34831, March 2018. ISSN 2050-084X. doi: 10.7554/eLife.34831. Publisher: eLife Sciences Publications, Ltd.
- Kevin A. Bolding and Kevin M. Franks. Recurrent cortical circuits implement concentration-invariant odor coding. *Science*, 361(6407):eaat6904, September 2018. doi: 10.1126/science.aat6904. Publisher: American Association for the Advancement of Science.
- Kevin A Bolding, Shivathimhai Nagappan, Bao-Xia Han, Fan Wang, and Kevin M Franks. Recurrent circuitry is required to stabilize piriform cortex odor representations across brain states. *eLife*, 9:e53125, July 2020. ISSN 2050-084X. doi: 10.7554/eLife.53125. Publisher: eLife Sciences Publications, Ltd.
- Claire Meissner-Bernard, Friedemann Zenke, and Rainer W Friedrich. Geometry and dynamics of representations in a precisely balanced memory network related to olfactory cortex. *bioRxiv*, pages 2023–12, 2023.
- D. A. Wilson, A. R. Best, and R. M. Sullivan. Plasticity in the Olfactory System: Lessons for the Neurobiology of Memory. *The Neuroscientist*, 10(6):513–524, December 2004. ISSN 1073-8584. doi: 10.1177/1073858404267048. Publisher: SAGE Publications Inc STM.
- Iori Ito, Rose Chik-ying Ong, Baranidharan Raman, and Mark Stopfer. Olfactory learning and spike timing dependent plasticity. *Communicative & Integrative Biology*, 1(2):170–171, 2008. ISSN 1942-0889.
- Teng-Fei Ma, Xiao-Lei Zhao, Lei Cai, Nan Zhang, Si-Qiang Ren, Fang Ji, Tian Tian, and Wei Lu. Regulation of Spike Timing-Dependent Plasticity of Olfactory Inputs in Mitral Cells in the Rat Olfactory Bulb. *PLOS ONE*, 7(4):e35001, April 2012. ISSN 1932-6203. doi: 10.1371/journal.pone.0035001. Publisher: Public Library of Science.
- Yaniv Cohen, Donald A. Wilson, and Edi Barkai. Differential Modifications of Synaptic Weights During Odor Rule Learning: Dynamics of Interaction between the Piriform Cortex with Lower and Higher Brain Areas. *Cerebral Cortex*, 25(1):180–191, January 2015. ISSN 1047-3211. doi: 10.1093/cercor/bht215.
- Gilad A. Jacobson, Peter Rupprecht, and Rainer W. Friedrich. Experience-Dependent Plasticity of Odor Representations in the Telencephalon of Zebrafish. *Current Biology*, 28(1):1–14.e3, January 2018. ISSN 0960-9822. doi: 10.1016/j.cub.2017.11.007. Publisher: Elsevier.
- Amit Kumar, Edi Barkai, and Jackie Schiller. Plasticity of olfactory bulb inputs mediated by dendritic NMDA-spikes in rodent piriform cortex. *eLife*, 10:e70383, October 2021. ISSN 2050-084X. doi: 10.7554/eLife.70383. Publisher: eLife Sciences Publications, Ltd.
- Yonatan Loewenstein, Annerose Kuras, and Simon Rumpel. Multiplicative Dynamics Under-

- lie the Emergence of the Log-Normal Distribution of Spine Sizes in the Neocortex In Vivo. *Journal of Neuroscience*, 31(26):9481–9488, June 2011. ISSN 0270-6474, 1529-2401. doi: 10.1523/JNEUROSCI.6130-10.2011. Publisher: Society for Neuroscience Section: Articles.
33. György Buzsáki and Kenji Mizuseki. The log-dynamic brain: how skewed distributions affect network operations. *Nature Reviews Neuroscience*, 15(4):264–278, 2014.
  34. M. C. W. van Rossum, G. Q. Bi, and G. G. Turrigiano. Stable Hebbian Learning from Spike Timing-Dependent Plasticity. *Journal of Neuroscience*, 20(23):8812–8821, December 2000. ISSN 0270-6474, 1529-2401. doi: 10.1523/JNEUROSCI.20-23-08812.2000. Publisher: Society for Neuroscience Section: ARTICLE.
  35. Yonatan Loewenstein, Uri Yanover, and Simon Rumpel. Predicting the Dynamics of Network Connectivity in the Neocortex. *Journal of Neuroscience*, 35(36):12535–12544, September 2015. ISSN 0270-6474, 1529-2401. doi: 10.1523/JNEUROSCI.2917-14.2015. Publisher: Society for Neuroscience Section: Articles.
  36. Yuansheng Zhou, Brian H Smith, and Tatyana O Sharpee. Hyperbolic geometry of the olfactory space. *Science advances*, 4(8):eaq1458, 2018.
  37. Tatyana O Sharpee. An argument for hyperbolic geometry in neural circuits. *Current opinion in neurobiology*, 58:101–104, 2019.
  38. Dmitri Krioukov, Fragkiskos Papadopoulos, Maksim Kitsak, Amin Vahdat, and Marián Boguná. Hyperbolic geometry of complex networks. *Physical Review E—Statistical, Nonlinear, and Soft Matter Physics*, 82(3):036106, 2010.
  39. Mark M Churchland, Byron M Yu, John P Cunningham, Leo P Sugrue, Marlene R Cohen, Greg S Corrado, William T Newsome, Andrew M Clark, Paymon Hosseini, Benjamin B Scott, et al. Stimulus onset quenches neural variability: a widespread cortical phenomenon. *Nature neuroscience*, 13(3):369–378, 2010.
  40. Yaniv Ziv, Laurie D. Burns, Eric D. Cocker, Elizabeth O. Hamel, Kunal K. Ghosh, Lacey J. Kitch, Abbas El Gamal, and Mark J. Schnitzer. Long-term dynamics of CA1 hippocampal place codes. *Nature Neuroscience*, 16(3):264–266, March 2013. ISSN 1546-1726. doi: 10.1038/nn.3329. Number: 3 Publisher: Nature Publishing Group.
  41. Dorgham Khatib, Aviv Ratzon, Mariell Sellevoll, Omri Barak, Genela Morris, and Dori Derdikman. Active experience, not time, determines within-day representational drift in dorsal CA1. *Neuron*, 111(15):2348–2356.e4, August 2023. ISSN 0896-6273. doi: 10.1016/j.neuron.2023.05.014. Publisher: Elsevier.
  42. Nitzan Geva, Daniel Deitch, Alon Rubin, and Yaniv Ziv. Time and experience differentially affect distinct aspects of hippocampal representational drift. *Neuron*, 111(15):2357–2366.e5, August 2023. ISSN 0896-6273. doi: 10.1016/j.neuron.2023.05.005.
  43. Daniel Deitch, Alon Rubin, and Yaniv Ziv. Representational drift in the mouse visual cortex. *Current Biology*, 31(19):4327–4339.e6, October 2021. ISSN 0960-9822. doi: 10.1016/j.cub.2021.07.062. Publisher: Elsevier.
  44. Michael E Rule, Adrianna R Loback, Dhruva V Raman, Laura N Driscoll, Christopher D Harvey, and Timothy O’Leary. Stable task information from an unstable neural population. *eLife*, 9:e51121, July 2020. ISSN 2050-084X. doi: 10.7554/eLife.51121. Publisher: eLife Sciences Publications, Ltd.
  45. Henry Markram, Joachim Lübke, Michael Frotscher, and Bert Sakmann. Regulation of Synaptic Efficacy by Coincidence of Postsynaptic APs and EPSPs. *Science*, 275(5297): 213–215, January 1997. doi: 10.1126/science.275.5297.213. Publisher: American Association for the Advancement of Science.
  46. Guo-qiang Bi and Mu-ming Poo. Synaptic Modification by Correlated Activity: Hebb’s Postulate Revisited. *Annual Review of Neuroscience*, 24(1):139–166, 2001. doi: 10.1146/annurev.neuro.24.1.139. \_eprint: <https://doi.org/10.1146/annurev.neuro.24.1.139>.
  47. Katherine Buchanan and Jack Mellor. The activity requirements for spike timing-dependent plasticity in the hippocampus. *Frontiers in Synaptic Neuroscience*, 2, 2010. ISSN 1663-3563.
  48. Matthieu Gilson and Tomoki Fukai. Stability versus Neuronal Specialization for STDP: Long-Tail Weight Distributions Solve the Dilemma. *PLOS ONE*, 6(10):e25339, October 2011. ISSN 1932-6203. doi: 10.1371/journal.pone.0025339. Publisher: Public Library of Science.
  49. Matthieu Gilson, Timothée Masquelier, and Etienne Hugues. STDP Allows Fast Rate-Modulated Coding with Poisson-Like Spike Trains. *PLOS Computational Biology*, 7(10): e1002231, October 2011. ISSN 1553-7358. doi: 10.1371/journal.pcbi.1002231. Publisher: Public Library of Science.
  50. Kristofer D. Carlson, Micah Richert, Nikil Dutt, and Jeffrey L. Krichmar. Biologically plausible models of homeostasis and STDP: Stability and learning in spiking neural networks. In *The 2013 International Joint Conference on Neural Networks (IJCNN)*, pages 1–8, August 2013. doi: 10.1109/IJCNN.2013.6706961. ISSN: 2161-4407.
  51. Felix Effenberger, Jürgen Jost, and Anna Levina. Self-organization in Balanced State Networks by STDP and Homeostatic Plasticity. *PLoS Computational Biology*, 11(9):e1004420, September 2015. ISSN 1553-734X. doi: 10.1371/journal.pcbi.1004420.
  52. Natalia Caporale and Yang Dan. Spike Timing-Dependent Plasticity: A Hebbian Learning Rule. *Annual Review of Neuroscience*, 31(1):25–46, 2008. doi: 10.1146/annurev.neuro.31.060407.125639. \_eprint: <https://doi.org/10.1146/annurev.neuro.31.060407.125639>.
  53. Abigail Morrison, Markus Diesmann, and Wulfram Gerstner. Phenomenological models of synaptic plasticity based on spike timing. *Biological Cybernetics*, 98(6):459, 2008. doi: 10.1007/s00422-008-0233-1. Publisher: Springer.
  54. Guo-qiang Bi and Mu-ming Poo. Synaptic Modifications in Cultured Hippocampal Neurons: Dependence on Spike Timing, Synaptic Strength, and Postsynaptic Cell Type. *Journal of Neuroscience*, 18(24):10464–10472, December 1998. ISSN 0270-6474, 1529-2401. doi: 10.1523/JNEUROSCI.18-24-10464.1998. Publisher: Society for Neuroscience Section: ARTICLE.
  55. Winston Haynes. Wilcoxon Rank Sum Test. In Werner Dubitzky, Olaf Wolkenhauer, Kwang-Hyun Cho, and Hiroki Yokota, editors, *Encyclopedia of Systems Biology*, pages 2354–2355. Springer, New York, NY, 2013. ISBN 978-1-4419-9863-7. doi: 10.1007/978-1-4419-9863-7\_1185.
  56. Marlene R. Cohen and Adam Kohn. Measuring and interpreting neuronal correlations. *Nature Neuroscience*, 14(7):811–819, July 2011. ISSN 1546-1726. doi: 10.1038/nn.2842. Number: 7 Publisher: Nature Publishing Group.

## Supplementary Note 1: Relation between the GMR process and Loewenstein et al.'s model

Let us begin by introducing the phenomenological model presented by Loewenstein et al. in (32), which describes the dynamics of the logarithm of the size of the  $k$ -th dendritic spine in a given synapsis,  $\tilde{X}^k$ , as a sum of two independent Ornstein-Uhlenbeck processes:

$$\log_{10}(\tilde{X}^k) = Y_1^k + Y_2^k + \log_{10} \tilde{\mu}. \quad (26)$$

In the above equation,  $\tilde{\mu}$  is the average of all spine sizes and  $Y_1^k$  and  $Y_2^k$  are OU processes described by:

$$\tau_i \frac{dY_i^k}{dt} = -Y_i^k + \sqrt{2\tau_i} \tilde{\sigma}_i \xi_i^k, \quad i = 1, 2 \quad (27)$$

where  $\xi_i^k$  is a Gaussian white noise such that  $\langle \xi_i^k \rangle = 0$  and  $\langle \xi_i^k(t) \xi_j^{k'}(t') \rangle = \delta_{i,j} \delta_{k,k'} \delta(t-t')$ . In the above model, the values for the timescales of the two processes,  $\tau_1$  and  $\tau_2$ , as well as their stationary variance,  $\tilde{\sigma}_1$  and  $\tilde{\sigma}_2$ , were fitted using empirical measures of the spine sizes in the dendrites of auditory cortex neurons recorded *in vivo* in mice. For our purposes, let us further simplify the above model considering that the dynamics is characterized by a single, most-relevant timescale, such that:

$$\ln(\tilde{X}^k) = Y^k + \ln \tilde{\mu}, \quad (28)$$

where, without loss of generality, we changed the decimal logarithm for the natural one to simplify the upcoming analysis.

Let us now go back to the stochastic differential equation for a geometric mean-reverting process:

$$\frac{dX^k}{dt} = \omega(\mu - X^k) + \sigma X^k \xi^k. \quad (29)$$

Applying Ito's Lemma to the function  $\ln(X^k)$ :

$$\frac{d(\ln(X^k))}{dt} = \omega \left( \frac{\mu}{X^k} - 1 \right) - \frac{1}{2} \sigma^2 + \sigma \xi^k. \quad (30)$$

In order to check the relation between the dynamics of both processes, let us assume that synaptic weights in our model,  $X^k$ , describe a magnitude proportional to the spine sizes empirically measured in (32) (i.e.,  $X^k \equiv \alpha \tilde{X}^k$ ). Therefore, using Eq. 28 we can approximate:

$$\frac{\mu}{X^k} \approx \frac{1 - Y^k}{\alpha}, \quad (31)$$

which, substituting in Eq. 30, leads to:

$$\frac{dY}{dt} = \omega \left( \frac{\mu}{\alpha \tilde{\mu}} (1 - Y^k) - 1 \right) - \frac{1}{2} \sigma^2 + \sigma \xi^k. \quad (32)$$

Comparing term by term with Eq. 27 for  $i = 1$ , and after several manipulations, one can finally see that both, the GMR process and the phenomenological model proposed in (32) (although reduced to a single timescale), follow identical equations under the following re-scaling of parameters:

$$\sigma = \sqrt{\frac{2}{\tau}} \tilde{\sigma} \quad (33)$$

$$\omega = \frac{1 - \tilde{\sigma}^2}{\tau} \quad (34)$$

$$\mu = \frac{\tilde{\mu} \alpha}{1 - \tilde{\sigma}^2}. \quad (35)$$

## Supplementary Note 2: The effects of learning-induced deterministic change in representation: A simple model

As we showed in the main text, changes in the neural representation of a particular odor occur through two mechanisms: learning induces synaptic changes towards the odor-specific sub-manifold in a deterministic fashion, whereas the stochastic weight dynamics causes random fluctuations akin to a Brownian motion. Here, we develop a simple model to demonstrate the interplay of these two mechanisms and show how they affect the measured representational “drift”.

Let us consider a two-dimensional representational space  $(x, y)$  such that, for a particular odor, the representational sub-manifold is a 1-D line at  $x = 0$ . Starting from an initial response  $(x_0, y_0)$  at time  $t = 0$ , the odor is presented at time  $t_i = (i - 1)\tau$  ( $i = 1, 2, \dots$ ), where  $\tau$  is the time interval between presentations. During the short presentation of the odor, the effect of learning drives the representation towards the representation sub-manifold, i.e., the  $x = 0$  line. Apart from these brief odor presentations, the representation changes randomly. To capture these two effects, we can formulate a simple model to describe the dynamics of the representation:

$$\frac{dx}{dt} = f(x) \sum_{i=1}^n \delta(t - t_i) + \eta_x(t), \quad (36)$$

$$\frac{dy}{dt} = \eta_y(t), \quad (37)$$

where the first term in the right-hand side of Eq. 36 represents the effects of learning during the brief odor presentation with  $f(x = 0) = 0$  and  $f'(x = 0) < 0$ , which guarantees that  $x = 0$  is the fixed line for the learning dynamics; while  $\eta_x(t)$  and  $\eta_y(t)$  are random white noises mimicking the effect of stochastic weight changes:  $\langle \eta_{x,y} \rangle = 0$ ,  $\langle \eta_x(t') \eta_x(t) \rangle = 2\Omega_x \delta(t - t')$ ,  $\langle \eta_y(t') \eta_y(t) \rangle = 2\Omega_y \delta(t - t')$ . For simplicity, we set  $f(x) = -\alpha x$  where  $\alpha > 0$  measures the strength of learning. We also assume  $\Omega_x = \Omega_y = \Omega$ , which is the strength of the random drift. The measured representational drift after  $n$  odor presentations or total time  $T = (n - 1)\tau$  is given by:  $\sigma^2 = \sigma_x^2 + \sigma_y^2$  where  $\sigma_x^2 \equiv \langle (x_0 - x(T))^2 \rangle$  and  $\sigma_y^2 \equiv \langle (y_0 - y(T))^2 \rangle$ .

In the direction normal to the representational sub-manifold (i.e., the  $y$ -direction) learning does not play any role and we have  $\sigma_y^2 = \Omega T$ . On the other hand, learning does play an important role in the  $x$ -direction and  $\sigma_x^2$  can be computed as follows. Denote the values of  $x$  before and after the odor presentation at time  $t_i$  as  $x_i^-$  and  $x_i^+$ , respectively. By integrating Eq. 36 from  $t_i^- = t_i - \epsilon$  to  $t_i^+ = t_i + \epsilon$  in an infinitesimal region around time  $t_i$  of the odor presentation, we have:  $\int_{t_i^-}^{t_i^+} \frac{dx}{x} = \ln(x_i^+ / x_i^-) = -\alpha$ , which leads to the equation for the “jump” process:

$$x_i^+ = e^{-\alpha} x_i^-. \quad (38)$$

Between two consecutive odor presentations, the dynamics is a pure diffusion process, and we have:

$$x_{i+1}^- = x_i^+ + \xi_i, \quad (39)$$

where  $\xi_i = \int_{t_i}^{t_{i+1}} \eta_x(t) dt$  is the displacement in  $x$  due to random weight change during time  $t_i$  to  $t_{i+1}$ . It is easy to show that  $\langle \xi_i \rangle = 0$  and  $\langle \xi_i^2 \rangle = \Omega \tau$ . Together with the initial condition,  $x_1^- = x_0$ , we can write:

$$x(T) \equiv x_n^+ = e^{-n\alpha} x_0 + \sum_{i=2}^n e^{-(n-i+1)\alpha} \xi_{i-1}, \quad (40)$$

from which we obtain:

$$\sigma_x^2 \equiv \langle (x_0 - x(T))^2 \rangle = x_0^2 (1 - e^{-n\alpha})^2 + \Omega \tau \frac{e^{-2\alpha} - e^{-2n\alpha}}{1 - e^{-2\alpha}}. \quad (41)$$

In the above expression, the first term comes from the deterministic changes of the neural activity from the initial position  $x_0$  towards the sub-manifold,  $x = 0$ ; whereas the second term comes from the random drift damped by learning. The behavior of  $\sigma_x^2$  in the absence or presence of learning is summarized below:

- In the absence of learning (i.e.,  $\alpha \rightarrow 0$ ), from Eq. 41 we have:  $\sigma_x^2 = \Omega \tau (n - 1) = \Omega T$ , which is just random diffusion as  $\sigma_x^2$  is linearly proportional to time.
- In the presence of learning (i.e., for a finite  $\alpha$ ) the measured “drift”,  $\sigma_x^2$ , is suppressed. Specifically, although  $\sigma_x^2$  increases with  $n$  transiently, it saturates to a constant when  $n\alpha \gg 1$ :  $\sigma_x^2 (n \gg \alpha^{-1}) = x_0^2 + \Omega \tau (1 - e^{-2\alpha})^{-1}$ .

Overall, even though learning suppresses drift at long time (or large values of  $n$ ), there may be an intermediate range of  $n$  where the drift measured by  $\sigma_x^2$  is actually bigger with a finite  $\alpha$ . The reason is that even though a finite  $\alpha$  always suppresses the second term in Eq. 41, it actually enhances the first term that is proportional to  $x_0^2$  (notice that the first term vanishes in the absence of learning). Therefore, depending on the initial distance to the representational sub-manifold,  $x_0$ , the deterministic changes towards the line  $x = 0$  can dominate the measured “drift”,  $\sigma_x^2$ , effectively making it larger than that without learning. This is what we refer to in the Discussion section of the main text as *fast drift* (41).

### Supplementary Note 3: Alignment of fast stimulus-induced drift with the directions of noise variability

As we showed throughout this work, the actual slow random drift, which we hypothesize stems from noisy multiplicative synaptic dynamics, affects the tuning of single neurons to a given set of stimuli (Fig.2i-j), thus affecting the measured *signal correlation* across days (i.e., pair-wise correlations between mean responses to different stimuli, see Fig.S.1k).

In contrast, *noise correlations* measure the observed co-variability in neural responses to the same stimulus repeated across different trials, under the same behavioral conditions (56). From an experimental point of view, the effects of STDP-induced changes—or, as we called it, the fast stimulus-dependent drift—, which can take place on a scale of milliseconds to seconds between trials, would emerge in long-recording experiments as part of this *noise variance* or trial-to-trial variability in the responses to the same stimulus set within a given test day.

Thus, if our hypothesis is right and the overall observed drift can have a contribution from fast, learning-induced dynamics at short time scales, then for every input and pair of recorded days, a general *drift vector* (pointing in the direction of population changes between such days in the N-dimensional space) should still have a small but significant projection in the directions encoding noise variability (see Fig. S.4a). Remarkably, this is exactly what Rule et al. observed when analyzing long-term calcium imaging recordings from mice in the mouse posterior parietal cortex (PPC) during a virtual reality T-maze task (44) (Fig.S.4b, gray box).

To test whether the same phenomenon can be captured with our model, we measured the alignment of the drift with the direction of maximum trial-to-trial variability by adapting the protocol introduced in (44). Let us define a *drift vector*,  $\Delta\vec{\mu}_{o,m}^{pq} = \mathbf{x}_{o,m,p} - \mathbf{x}_{o,m,q}$ , as the trial-conditioned change in the mean firing rate response of the population to odor  $o$ , during trial  $m$ , between days  $p$  and  $q$ . We now compute, for each odor,  $o$ , the noise or trial-to-trial covariance matrix on the first test day,  $\Sigma_o$ , and define an statistic that determines the amount of overlapping between the drift vector and the noise encoding direction as:

$$\phi_{o,m}^{pq} = \frac{\Delta\vec{\mu}_{o,m}^{pq \top} \Sigma_o \Delta\vec{\mu}_{o,m}^{pq}}{\lambda_{max} |\Delta\vec{\mu}_{o,m}^{pq}|^2}, \quad (42)$$

where we normalized the drift vector to unit length and divided by the maximum eigenvalue,  $\lambda_{max}$ , of the noise covariance matrix. Thus, the above statistic provides a measure of the amount of drift that can be explained (or overlaps) with the principal direction of noise correlations, being one if both vectors align perfectly, and zero if they are completely orthogonal (44). Finally, to discount for the expected chance alignment that can take place between any two random vectors in an  $N$ -dimensional space,  $\psi_0 = \langle \text{tr}(\Sigma_o) / (N\lambda_{max}) \rangle$  (where the average is taken over all odors, see also (44) for more details), we compute a corrected final estimate as:

$$\rho_{o,m}^{pq} = \frac{\phi_{o,m}^{pq} - \psi_0}{1 - \psi_0}. \quad (43)$$

Figure S.4b shows the distribution of the above measure across all trials and odors, for the case in which we have unfamiliar odors presented every 8 days (red boxplot) and familiar odors presented every day (blue boxplot). As we can see, non trivial overlapping is observed for representations of familiar odors, in which the presentation of the stimulus “pulls back” the weights towards the submanifold previously learned during the familiarization process. The same quantity for the PPC, as measured in (44), is shown for comparison purposes (gray boxplot).



## Supplementary Figures

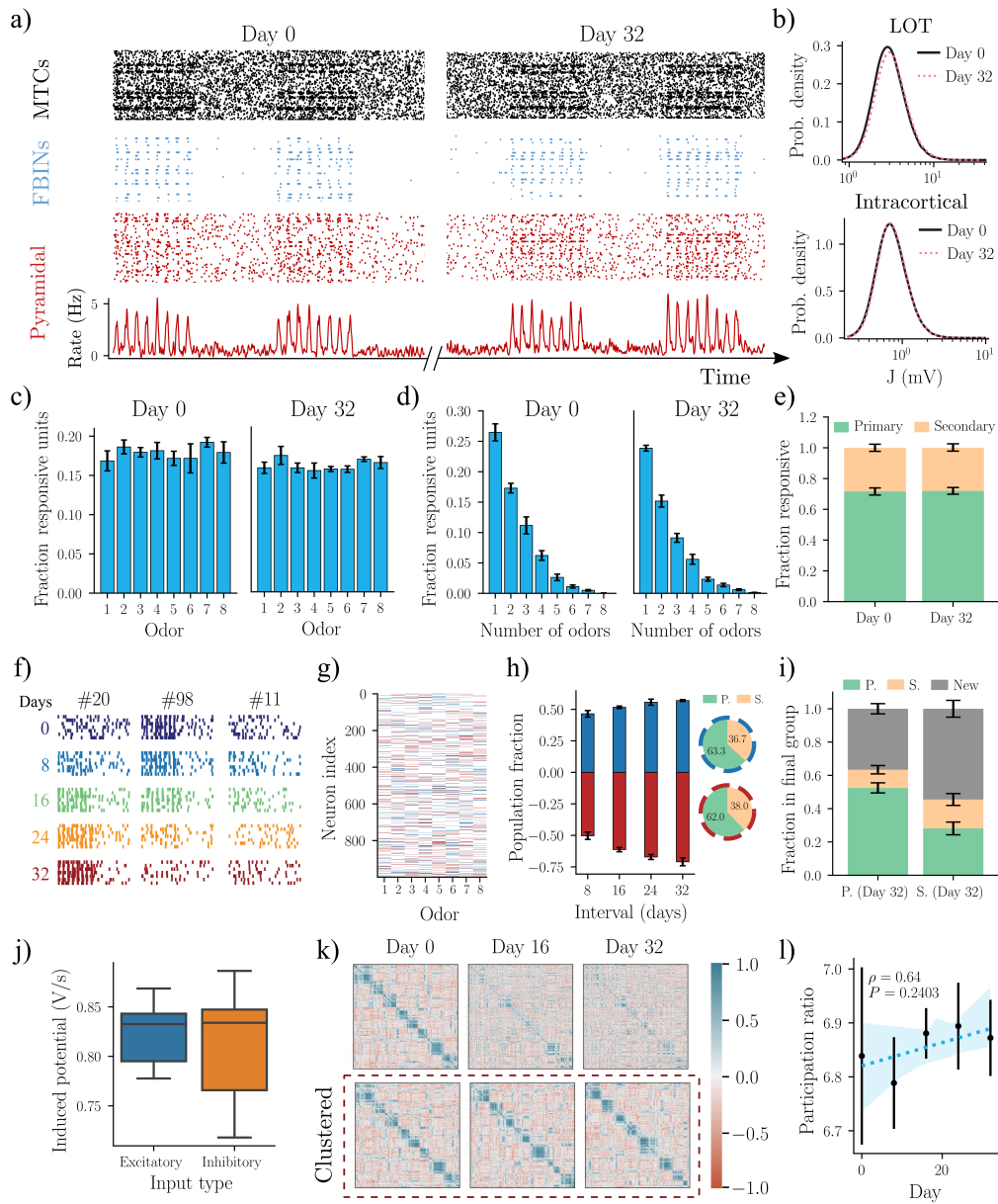


**Fig. S.1. Extended results on the effects of representational drift.** (a) Raster plots for a sub-sample (10%) of each neural population during two trials of an odor presentation on day 0 and day 32, together with the corresponding pyramidal population average firing rate. (b) Lognormal probability distributions for MTC-to-pyramidal (top) and pyramidal-to-pyramidal (bottom) weights. (c) Fraction of pyramidal neurons that respond to each odor. (d) Fraction of pyramidal neurons responsive to exactly  $n$  odors. (e) Fraction of primary and secondary labels within responsive units. (f) Raster plots for the same three odor-unit pairs in Fig. 2j across test days. Each row represents a single trial of odor presentation. (g) Changes in neuron selectivity after 32 days (blue=gain; red=loss) to each odor with respect to the beginning of the experiment. (h) Left: fraction of units that gained (blue) or lost (red) responsiveness, relative to the total number of initially responsive units. Right, top: fraction of primary and secondary labels for all units responsive on last but not first test day. Right, bottom: same as previous, but for all units responsive on first but not last day. (i) Composition of primary and secondary sets on day 32 in terms of unit classes on day 0. (j) Change to pyramidal membrane potential from excitatory (blue) and inhibitory (orange) sources over 1s, illustrating the existing balance between excitation and inhibition in our model. (k) Pearson's correlation matrices for pyramidal responses on three test days, with units clustered by correlation on day 0 (top), or correlation in each test day (bottom). (l) Dimensionality (as measured by the normalized participation ratio) of drifting representation manifold, averaged over  $n = 6$  experiments (mean  $\pm$  std, shaded blue area: 95% CI for regression).

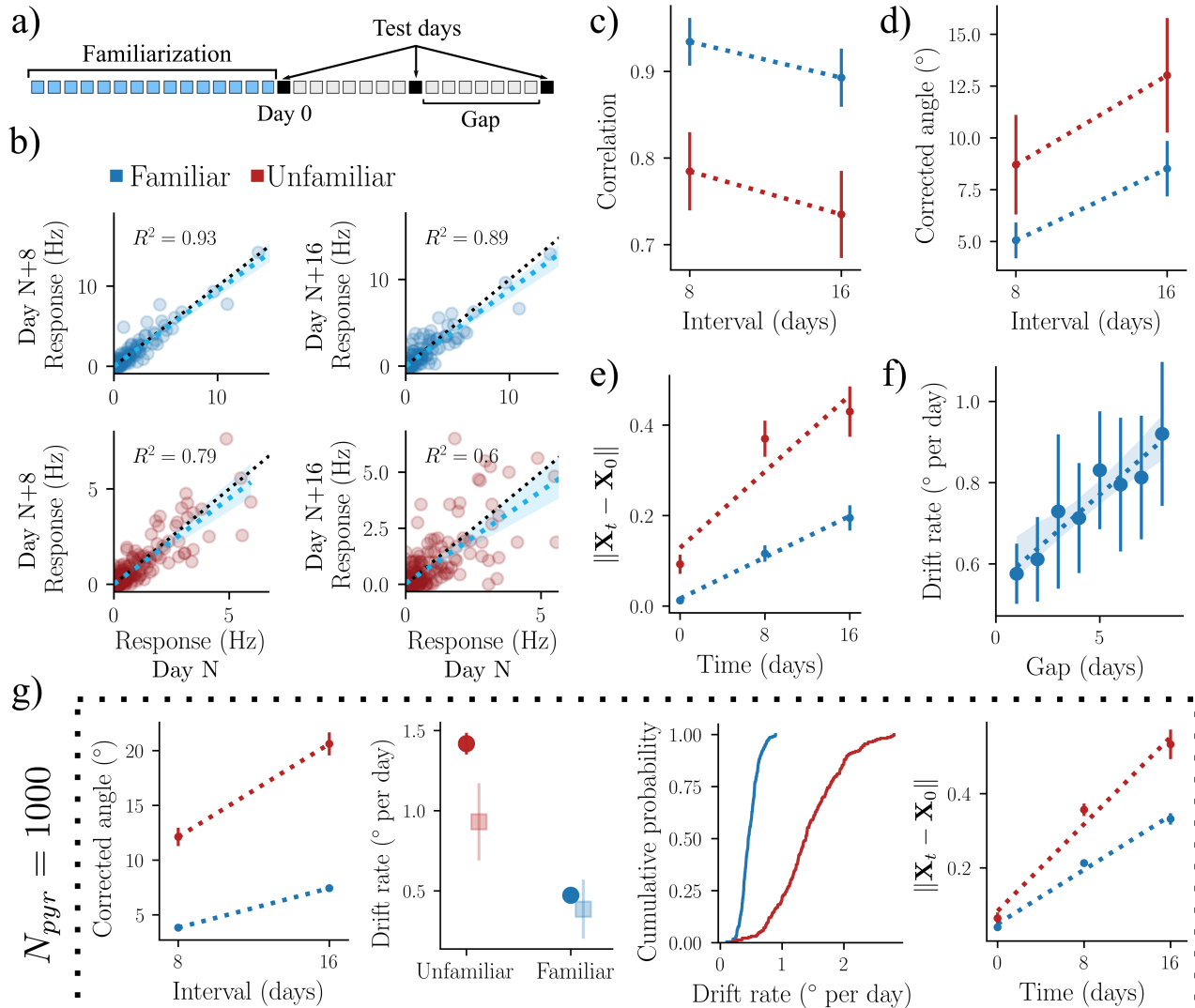


**Fig. S.2. Extended results on the effects of learning.** In all panels, unless otherwise stated, simulations mimic experiments with Cohort A, with blue (red) denoting familiar (unfamiliar) odors. **(a)** Schematic depiction of a typical simulated experiment. **(b)** Regression of firing rate responses across 8- to 32-days intervals for 100 randomly chosen odor-unit pairs. **(c)** Average population vector correlation and **(d)** average corrected angle between same-odor representations across intervals between test days. **(e)** Euclidean distance between same-odor representations across test days, averaged over odors and trials, and normalized by average within-day distance for different odor representations. **(f)** Average drift rate in degree angles per day for simulations interpolating between Cohort A (odors presented every day, first point) and Cohort B (odors presented every 8 days, last point). **(g)** From left to right: corrected angle, average drift rate, cumulative probability distribution and Euclidean distance between same-odor representations for a network with  $N = 1000$  pyramidal neurons.

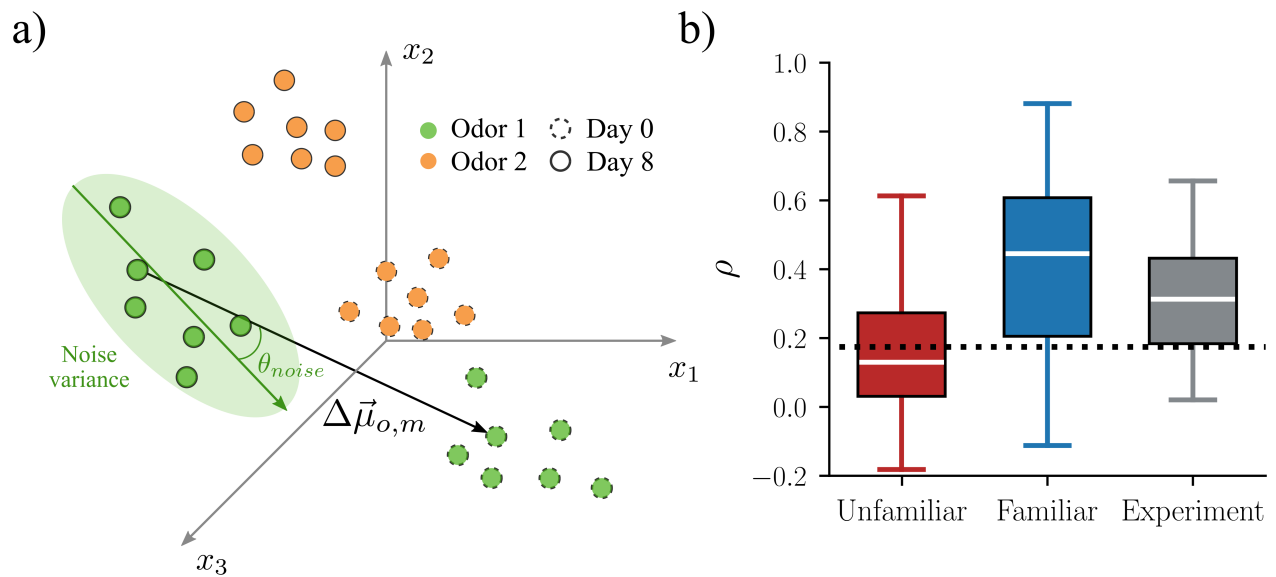


**Fig. S.3. A simple model for the interplay between learning and drift.** (a) Trajectories in the  $(x, y)$  representational space for the model described by Eqs. 36-37 with a “learned” submanifold at  $x = 0$  (green dashed line) and two different initial conditions:  $x_0 = 0.25$  (blue) and  $x_0 = 1$  (orange). For each initial configuration (square marker), we ran simulations with  $(\alpha = 0.05)$  and without  $(\alpha = 0)$  learning. Star markers point to the end of the trajectories. (b) As in (a), but now we plot the distance to the  $x = 0$  sub-manifold against the simulated time. (c) Solution to Eq. 41 for an initial condition  $x_0 = 1$ , with learning  $(\alpha = 0.05)$ , green line) and without learning  $(\alpha = 0)$ , black dotted line). In all simulations:  $T = 1000\text{s}$ ,  $\tau = 1\text{s}$ ,  $\Omega = 0.01$ ,  $y_0 = 0.5$ . For plots in (a) and (b), trajectories are integrated with a time step  $dt = 0.002$  and sampled every 500 steps.

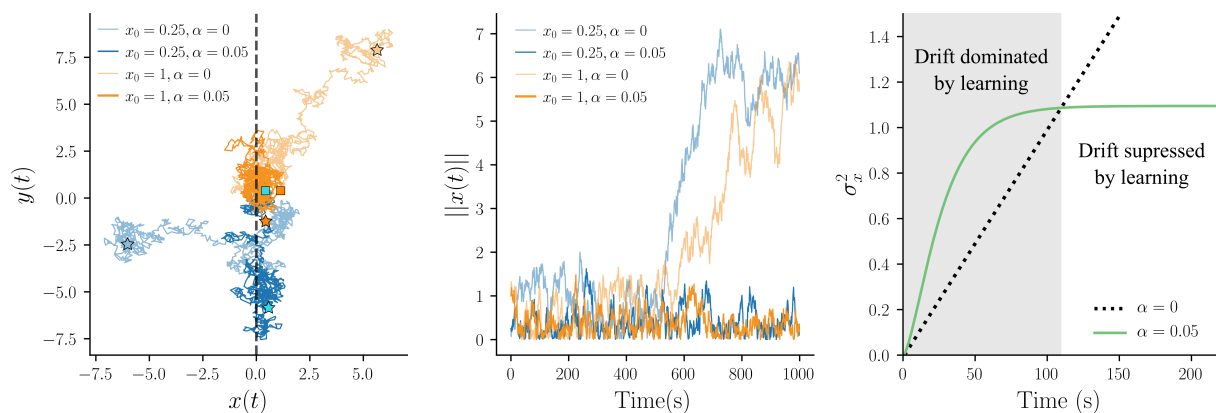


**Fig. S.4. Drift alignment with “noise” variability** (a) Drift (black arrow) and noise (green arrow) directions in a 2-dimensional subspace spanned by population responses to two odors: each circle represents population mean activity on a single trial. For each pair of test days, given an odor,  $o$ , and trial,  $m$ , a drift vector  $\Delta\vec{\mu}_{o,m}$  can be defined between the trial-conditioned population vectors. (b) Drift alignment with noise direction averaged over all unfamiliar odors, presented every 8 days (red); over all familiar odors, presented every day (blue); and the same quantity for the empirical measure in Rule *et al.* (44). Dotted black line shows the expected chance alignment for two random vectors in an  $N$ -dimensional space.